THESIS FOR THE DEGREE OF DOCTOR OF PHILOSOPHY

Estimating the Air-Water Gas Transfer Velocity during Low Wind Conditions

SAM TORE FREDRIKSSON

UNIVERSITY OF GOTHENBURG
FACULTY OF SCIENCE

DOCTORAL THESIS
UNIVERSITY OF GOTHENBURG
DEPARTMENT OF MARINE SCIENCES
GOTHENBURG, SWEDEN 2016

ISBN (Print): 978-91-628-9798-7
ISBN (PDF): 978-91-628-9799-4

Sam Tore Fredriksson
Estimating the Air-Water Gas Transfer Velocity during Low Wind Conditions

ISBN(Print): 978-91-628-9798-7
ISBN (PDF): 978-91-628-9799-4
Internet-ID: http://hdl.handle.net/2077/41805
Printed by Ineko AB

Distribution: Department of Marine Sciences, University of Gothenburg, Sweden

Abstract

The abundances of atmospheric carbon dioxide, CO_2, and methane, CH_4, are increasing. These increases affect e.g., the global carbon cycle and the climate both regionally and globally. To better understand the present and future atmospheric CO_2 and CH_4 concentrations and their climate impact, the gas exchange between water and the atmosphere is important. This exchange can occur in two directions. Oceans take up approximately one third of the anthropogenic CO_2 release (the ocean carbon sink). At the same time coastal waters and inland waters emit large amounts of CO_2 and CH_4, altogether corresponding to a similar amount as the ocean sink.

The interfacial gas-flux for CO_2 and CH_4 is controlled by the water-side. The gas-flux, F_g, is for such gases typically estimated as $F_g = k_g(C_{wb} - \vartheta C_{\mathrm{as}})$ where k_g is the gas transfer velocity, C_{wb} and C_{as} are the gas concentrations in the water bulk and in the air at the surface, and ϑ is the dimensionless Ostwald solubility coefficient. The subject of this thesis is to describe and estimate k_g for gases that have a water-side controlled gas-flux (e.g., CO_2, and CH_4). Besides being important for the geophysical sciences, k_g is also used to design and optimize many applications in e.g., chemical and environmental engineering.

The transfer velocity is influenced by interfacial shear stress from wind, natural convection due to surface heat flux, microscale breaking waves at moderate wind speeds, breaking waves at high wind speeds, bubbles, surfactants, and rain. This thesis focuses on the low wind condition where the forcings due to shear stress, natural convection, and surfactants are important. The relative importance of buoyancy and shear forcing is characterized via a Richardson number $Ri = B\nu/u_*^4$. Here B, ν, and u_* are the buoyancy flux, kinematic viscosity, and friction velocity, respectively. The thesis summarizes three papers where k_g has been studied numerically with direct numerical simulations (DNS) and one paper where field observations have been used.

The results from the field measurements show close relationships for the method using flux-chambers and the parameterization using the rate of turbulent kinetic energy dissipation, and the quantities surface rms velocity and the significant wave height. A parameterization of area-integrated values of k_g from wave measurements was proposed.

The DNS comprise flow conditions ranging from convection-dominated to shear-dominated cases. The results are used to: (i) evaluate different parameterizations of the air-water gas-exchange, (ii) determine, for a given buoyancy flux, the wind speed at which gas transfer becomes primarily shear driven, (iii) find an expression for the gas-transfer velocity for flows driven by both convection and shear, and (iv) investigate the influence of surfactants on gas transfer velocity.

Parameterizations using either the rate of turbulent kinetic energy dissipation or the horizontal surface flow-divergence show a larger disadvantageous dependence on the type of forcing than the parameterization using the surface-normal heat-flux. Two parametrizations using the wind-speed above the surface give reasonable estimates for the transfer-velocity, depending however on the surface heat-flux. The transition from convection- to shear-dominated gas-transfer-velocity is shown to be at $Ri \approx 0.004$. This means that buoyancy fluxes in natural conditions are not important for gas exchange at wind velocities U_{10} above approximately $3\ ms^{-1}$. Below this wind speed the buoyancy fluxes should be taken into account.

The transfer velocity is shown to be well represented by two different approaches: (i) Additive forcing as $k_{g,sum} = A_{Shear}u_*(Ri/Ri_c + 1)^{1/4}Sc^{-n}$, where $Ri_c = \left(A_{Shear}/A_{Buoy}\right)^4$ is a critical Richardson number, and (ii) either buoyancy or shear-stress forcing that gives $k_g = A_{Buoy}(B\nu)^{1/4}Sc^{-n}$ for $Ri > Ri_c$ and $k_g = A_{shear}u_*Sc^{-n}$ for $Ri < Ri_c$. Here $A_{Buoy} = 0.4$ and $A_{Shear} = 0.1$ are constants, $Sc = \nu/D$ is the Schmidt number, D is the gas diffusivity in water, and n is an exponent that depends on the water-surface characteristics.

Keywords: air-sea gas exchange, turbulence, heat flux, natural convection, shear, direct numerical simulations, gas transfer velocity, IR, flux-chambers

Populärvetenskaplig sammanfattning

Mängden växthusgaser såsom koldioxid och metan ökar i atmosfären. Ökningen påverkar bland annat vårt klimat såväl globalt som regionalt och även jordens kretslopp av kol.

Eftersom naturen strävar efter jämvikt leder skillnaden i koncentration mellan hav och luft till en transport i riktning mot koncentrationsunderskottet. En ökning av koldioxidhalten i atmosfären leder alltså till en ökning av mängden kol i jordens vattendrag och vice versa.

Mängden kol påverkar i sin tur exempelvis vattnets surhet vilket gör att livet i havet förändras och påverkar de organismer som finns i havet och dess närhet.

Förändringar i klimatet leder till förändrade temperaturer i hav och sjöar vilket i sin tur växelverkar med både klimatet och med hur snabbt koncentrationsutjämningen mellan atmosfär och hav sker. Denna växelverkan är komplex och för att öka förståelsen för hur ökade halter av växthusgaser påverkar jorden är modeller i stor och liten skala bra hjälpmedel.

För att ge trovärdiga och användbara resultat krävs att viktiga processer är modellerade så korrekt som möjligt. En sådan viktig process är med vilken hastighet en ojämvikt i koncentrationen mellan luft och vatten utjämnas. Denna hastighet beskrivs ofta som en övergångshastighet för olika gaser. Denna avhandling handlar om att kunna beskriva och modellera denna övergångshastighet (för vattenlösliga gaser för vilka gasflödet kontrolleras av vattensidan, såsom koldioxid och metan) så korrekt som möjligt.

Övergången mellan vattenlöst koldioxid och koldioxid i luften sker genom molekylär diffusion och kan beskrivas med hjälp av Ficks lag där flödet bestäms av gasens diffusionskoefficient multiplicerad med gasens koncentrationsgradient precis under vattenytan.

Då det gäller koldioxidtransport genom en vattenyta beror koncentrationsgradienten till stor del på hur effektiv transporten av koldioxiden är i vattnet, vilket beror på att koldioxid blandar sig mycket långsammare i vatten än i luft. Gasflödets flaskhals blir alltså vattnet.

Gasens koncentrationsutjämning med hjälp av enbart diffusion, som kan ses som koncentrationsutjämning i en helt stillastående vätska, är en mycket långsam process medan koncentrationsutjämning med hjälp av rörelser (turbulens) i vattnet är betydligt snabbare. Turbulensens intensitet påverkas av konvektion på grund av temperaturskillnader i vattnet, vågor, hastighetsvariationer i vattnet på grund av vind, strömmar i vattnet, regn, bubblor, bottenegenskaper och eventuell ytfilm vilken framförallt påverkar vattnets ytspänning.

I detta arbete studerar vi övergångshastigheten som funktion av naturlig konvektion, vind (vid relativt låga vindhastigheter), djup, ytfilm och vågor. Studien har utförts med hjälp av fältmätningar vid Bornö forskningsstation i Gullmarsfjorden, men framförallt genom numerisk modellering.

Resultaten kan sammanfattas i att övergångshastigheten vid låga vindhastigheter kan beskrivas med hjälp av naturlig konvektion i vattnet och den skjuvkraft med vilken vinden påverkar vattenytan. Resultaten visar vidare att ett Richardson-tal kan används för att bestämma om det är drivningen från konvektion eller skjuvning som är dominerande för drivningen av gasflödet. Konvektionen påverkar övergångshastigheten upp till cirka 3 m/s. Resultaten bekräftar också ett tydligt samband mellan övergångshastigheten, gasens diffusionshastighet i vattnet och ytfilmens egenskaper.

Preface

This thesis consists of a synthesis in Part A and four appended publications in Part B. The publications are referred to in the text by their Roman numbers. The published or accepted publications are reprinted with permission from respective journal.

I. Fredriksson, S.T., Handler, R.A., Nilsson, H., Zhang, Q., and Arneborg, L. (2016) **An Evaluation of Gas Transfer Velocity Parameterizations During Natural Convection using DNS.** Journal of Geophysical Research: Oceans. doi: 10.1002/2015JC011112
Fredriksson performed the modelling and all data analysis, had a leading role in writing the text and prepared all figures.

II. Zhang, Q., Handler, R.A., and Fredriksson, S.T. (2013) **Direct numerical simulation of turbulent free convection in the presence of a surfactant.** International Journal of Heat and Mass Transfer. doi: 10.1016/ j.ijheatmasstransfer.2013.01.031
Fredriksson had a minor role in writing, discussed the conclusions, and commented the text

III. Fredriksson, S.T., Handler, R.A., Nilsson, H., and Arneborg, L. (2016) **Surface Shear Stress Dependence of Gas Transfer Velocity Parameterizations using DNS.** Submitted 2016.
Fredriksson performed the modelling and all data analysis, had a leading role in writing the text and prepared all figures.

IV. Gålfalk, M., Bastviken, D., Fredriksson, S.T., and Arneborg, L. (2013) **Determination of the piston velocity for water-air interfaces using flux chambers, acoustic Doppler velocimetry, and IR imaging of the water surface.** Journal of Geophysical Research: Biogeosciences, doi: 10.1002/jgrg.20064
Fredriksson had a minor role in writing, discussed the conclusions, and commented the text

Peer reviewed publications not included in this thesis:

Andric, J., Fredriksson, S. T., Lindstrom, S. B., Sasic, S., and Nilsson, H. (2013) **A study of a flexible fiber model and its behavior in DNS of turbulent channel flow.** Acta Mechanica. doi: 10.1007/s00707-013-0918-y

Fredriksson, S.T., Arneborg, L., Nilsson H., and Handler, R.A. (2015). **Near-surface physics during convection affecting the air-water gas transfer.** Proceedings of 7th International Symposium on Gas Transfer at Water Surfaces, Seattle, USA.

TABLE OF CONTENTS

Part A. Synthesis

Part B. Paper I-IV

Part A

Synthesis

1 INTRODUCTION

The concentrations of atmospheric carbon dioxide (CO_2) and methane (CH_4) are increasing. This affects e.g., the climate of the earth and results, through air-water gas exchange, also in an acidification of aquatic systems such as oceans, lakes, and watercourses. The gas concentration and the gas exchange vary, however, largely both temporally and spatially (Figure 1) and an increased knowledge of the transport and accumulation processes of CO_2 and CH_4 is increasingly important in order to be able to make more precise predictions of the future climate and the aquatic environment. Recent research has e.g., updated the global carbon cycle estimates (Figure 2), resulting in the insight that the gas-exchange from inland waters plays a much larger role than previously believed [*Bastviken et al.*, 2011; *Ciais et al.*, 2013; *Tranvik et al.*, 2009]. These predictions are often based on numerical global and regional models where the gas flux F_g usually are estimated as a product of a gas transfer velocity, k_g, and the gas concentration difference between the water and air. The uncertainty in the estimations of k_g is though still large for low wind conditions, typically found in inland waters and occasionally in the oceans. Typical areas with low average wind speeds in the oceans are found e.g., along the equator [*Monahan*, 2006]). This thesis discusses what affects k_g during low wind conditions and presents new parameterizations which can be used to estimate it.

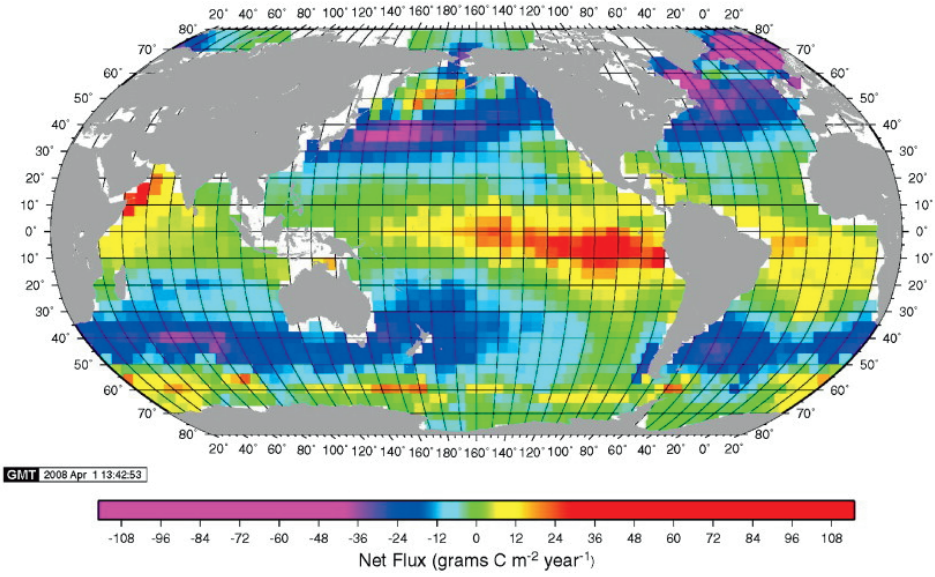

Figure 1. Estimated carbon dioxide flux averaged over year 2000. (Figure 13 in [Takahashi et al., 2009])

The introduction will continue with a more thorough background description, and a motivation for the need of further understanding of the gas-exchange. Then the gas transfer velocity will be defined and the processes that affect it will be discussed. The introduction is closed by presenting some of the parametrizations presently being used. Section 2 describes the numerical and field-measurement methods used in the papers that constitute this thesis. The main contributions of the work are presented in section 3. Finally, the conclusions and future perspectives are given in section 4.

1.1 Background and thesis motivation

Figure 3 shows a classic diagram in the context of climate change and the abundance of greenhouse gases. The measurements are carried out at Mauna Loa at Big Island, Hawaii. It represents the longest continuous measurement series of the atmospheric concentration of CO_2 and it shows a continuous increase of the annual averages all the way from the beginning of the measurements. The black curve is the yearly mean while the blue curve shows the yearly variation. Similarly, recordings of the concentration of atmospheric CH_4 show a steady increase (approximately 10% since 1988). An increase of atmospheric CO_2 affects the aquatic systems by changing the balance of dissolved CO_2 in the water. Although the increase naturally is affects land based processes as well, these are not further treated in this thesis. Furthermore, it is affecting the global climate. Different regional and global models are used to enhance the knowledge of how this increase affects the world now and in the future. Figures 1 and 2 show two examples of results from global models where Figure 1 shows the spatial distribution of the mean carbon dioxide flux for the year 2000 [*Takahashi et al.*, 2009] and Figure 2 shows an estimate of the global carbon cycle where the red arrows manifest the anthropogenically changed carbon fluxes and reservoir masses [*Ciais et al.*, 2013].

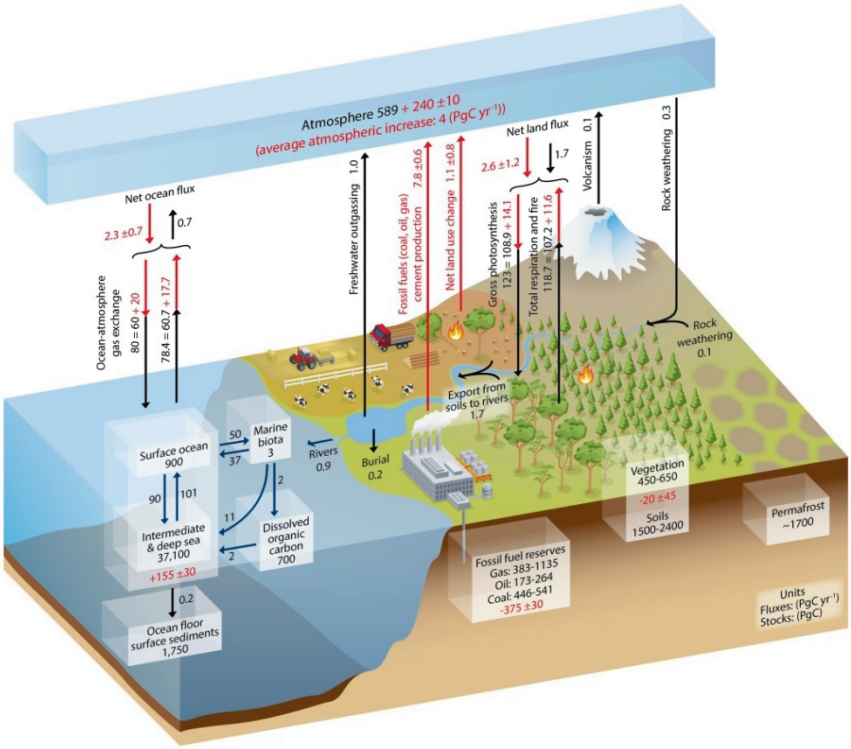

Figure 2. "Simplified schematic of the global carbon cycle. Numbers represent reservoir mass, also called 'carbon stocks' in PgC ($1\ PgC = 10^{15} gC$) and annual carbon exchange fluxes (in $PgC\ y^{-1}$). Black numbers and arrows indicate reservoir mass and exchange fluxes estimated for the time prior to the industrial Era, about 1750... Red arrows and numbers indicate annual 'anthropogenic' fluxes averaged over the 2000-2009 time period..." (Figure 6.1 in IPCC 2013 [Ciais et al., 2013]).

The work summarized in this thesis aims at improving: (i) numerical model performance, (ii) monitoring of gas exchange in water bodies, and (iii) the understanding of the processes involved in interfacial gas exchange. The common method to estimate the air-water gas-exchange in both regional and global models is to multiply a gas transfer velocity with the gas concentration difference in the water and in the atmosphere. In turn, the gas transfer velocity is often estimated as a function of the wind speed. Although the wind speed is important for the gas-exchange, it cannot, especially during low wind conditions, be used alone to estimate the transfer velocity without missing out other important factors, such as water-side natural convection and surfactants. This is also manifested through a widely varying magnitude of k_g between different parameterizations [*Bade*, 2009; *Takahashi et al.*, 2009; *Wanninkhof et al.*, 2009]. The first goal of the work summarized in this thesis is therefore to provide a better parameterization of the gas transfer velocity to regional and global models.

On a smaller scale, it is also important to be able to understand the processes in smaller water bodies e.g., lakes, streams, and coastal waters. The gas flux is difficult to measure directly, whereas measuring secondary quantities (to be used for the flux estimation) such as the gas concentration in the water, surface heat flux, and wind speed are easier. The second goal is therefore to improve methods for monitoring and estimating fluxes based on secondary quantities. These estimates can then beside improving the understanding of the actual water body also be used to aggregate better estimates of the global gas-exchange. It can e.g., be noted that the freshwater outgassing that was not included in the previous assessment by IPCC is of the same order of magnitude as the net ocean gas flux (Figure 2).

The third goal with this thesis is to enhance the understanding of the small-scale processes present in the vicinity of the air-water interface. This understanding of air-water gas transfer can also be used outside the geophysical sciences, e.g., in chemical and environmental engineering [*Jahne and Haussecker*, 1998].

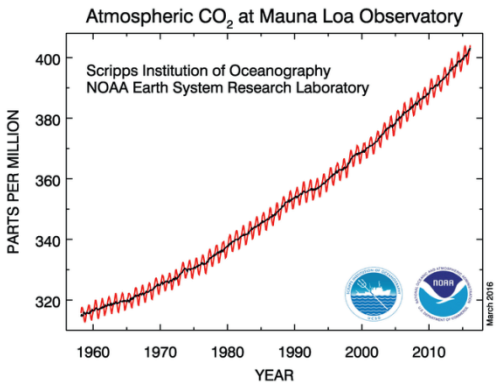

Figure 3. Recorded concentrations of atmospheric carbon dioxide from 1958 up to now at Mauna Loa, Hawaii, USA. [Dr. Pieter Tans, NOAA/ESRL (www.esrl.noaa.gov /gmd/ccgg/trends/) and Dr. Ralph Keeling, Scripps Institution of Oceanography (scrippsco2.ucsd.edu/)]

1.2 Gas exchange principles

The factors that influence the gas exchange across an air-water interface can be divided into (i) physical factors, i.e., advective/turbulent and molecular transport processes and (ii) biochemical factors (however, not considered in this thesis) which typically are biochemical or biological processes that either produce or consume gas. The transfer velocity for the two greenhouse gases CO_2 and CH_4 is controlled (limited) by the water side meaning that the flux is mainly limited by physical transport processes in the water [*Jahne and Haussecker*, 1998]. As a note it can be mentioned that the transfer of many other common properties such as heat, momentum and water vapor are controlled by the air side. The present work does only consider water-side-controlled gases and hence only the transport processes at the water side. The physical factors that influence the exchange of these gases (controlled by the water-side) comprise e.g., interfacial shear due to wind forcing, microscale breaking waves at moderate wind speeds, breaking waves at high wind speeds, bubbles, raindrops, surfactants, and convection due to surface heat loss [*Macintyre et al.*, 2002].

The actual interfacial gas-exchange is, neglecting the effects of bubbles or raindrops, maintained by pure molecular diffusion driven by the gas concentration gradient just below the air-water interface. A diffusive boundary layer (Figure 4) is formed above a turbulent layer where the turbulent motions are attenuated due to viscous damping and the presence of the surface. This diffusive gas exchange in this layer can be estimated by Fick's law

$$F_g = -D\frac{\partial C}{\partial z}, \qquad (1)$$

where D is the molecular diffusivity and $\partial C/\partial z$ is the vertical concentration gradient (Figure 4). Even though the gas exchange is a molecular diffusive process in the diffusive boundary layer, the magnitude of the diffusive exchange is highly dependent on the turbulence below. This is since besides being the main transport agent in the turbulent layer, the turbulence is also to a large degree influencing the molecular diffusive transport by affecting the diffusive boundary layer thickness, δ. Intense turbulence and advective motions result in a thinner δ, a larger concentration gradient $\partial C/\partial z$ and hence a higher gas exchange.

1.3 Forcing by wind and natural convection

In this thesis we focus on the forcing from interfacial shear due to wind shear and natural convection due to surface heat loss since they are important during low wind conditions. A schematic of these forcings is shown in Figure 4.

The air-water velocity difference causes a shear stress, τ_0, at the air-water interface. This shear stress results in a momentum exchange between the air and water, thereby affecting the velocity and turbulence intensity in both. This exchange is in the numerical simulations modeled with a constant shear stress at the surface boundary assuming steady wind conditions and no waves, spray, bubbles, or rain.

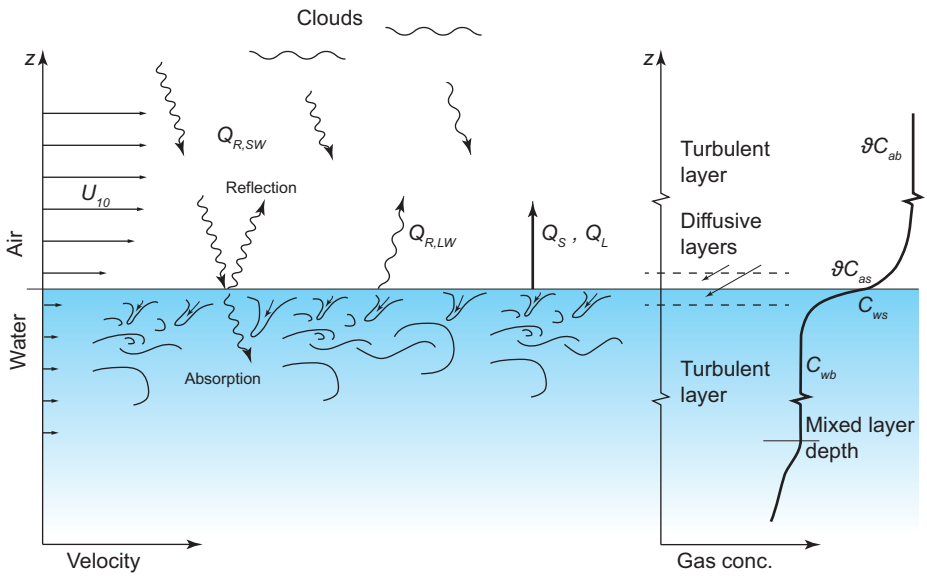

Figure 4. Conceptual diagram of air and water velocity, heat fluxes, and mean gas concentration in the air and water. Sensible heat flux, Q_S, latent heat flux, Q_L, and net longwave radiation, $Q_{R,LW}$, originate from the water surface whereas the shortwave solar radiation, $Q_{R,SW}$, penetrates the surface. U_{10} is the wind speed 10 *m above the water surface. C_{wb}, C_{ws}, C_{ab}, and C_{as} are the bulk and surface gas-concentrations in the water and air, respectively. ϑ is the dimensionless Ostwald solubility coefficient. Advective transport dominates in the turbulent layers, whereas diffusive transport dominates in the very thin diffusive boundary layers (note the different vertical scale for the velocity gradient and the gas concentration represented with a broken z-axis in the vertical direction, e.g., the diffusive boundary layer thickness for CO_2 and CH_4 in water is typically of the order of 1 mm or less).*

The wind speed is often referred to as U_{10} which is the wind speed at 10 m above the water surface. In order to express the applied τ_0 in U_{10}, the equation

$$\frac{\mathrm{U(z)}}{\mathrm{u_{*a}}} = \kappa^{-1}\ln\left(\frac{z\cdot u_{*a}}{\nu_a}\right) + 5.7 \qquad (2)$$

can be used for neutral conditions [*Csanady*, 2001]. Here the subscript a denote the air side, z is the height above the air-water interface, κ is the von Karman constant, and ν_a is the air-side kinematic viscosity. The water-side and air-side friction velocity is related as $u_* = u_{*a}(\rho_a/\rho)^{1/2}$ where ρ_a and ρ are the densities of air and water. The applied shear stresses, $\tau_0 = \rho u_*^2$, in the DNS cases in the present work correspond to U_{10} up to approximately 2 ms^{-1} according to Equation (2). Without going into too much detail it can be said that stable air conditions (meaning a negative buoyancy flux in the air, i.e., decreasing density with height) decrease the turbulence intensity in the air, while an unstable increases it. This results in that a higher U_{10} is required in order to maintain the same u_{*a} for stable compared to neutral conditions [*Csanady*, 2001; *Garratt*, 1992]. Similarly a lower U_{10} is required in order to maintain the same u_{*a} for unstable compared to neutral conditions.

The net heat flux at the air-water interface can be written as

$$Q_0 = Q_S + Q_L + Q_{R,LW}, \quad (3)$$

where the sensible heat flux Q_S is driven by the temperature difference between the water and air, the latent heat flux Q_L by water evaporation, and the radiative heat flux $Q_{R,LW}$ by longwave radiative transfer. The radiative heat flux is here decomposed into shortwave, $Q_{R,SW}$, originating from the solar irradiance and longwave radiative fluxes, $Q_{R,LW}$. Q_S, Q_L, and $Q_{R,LW}$ originate from the uppermost molecular layers of the water whereas $Q_{R,SW}$ penetrates the surface. The penetration depth of $Q_{R,SW}$ depends on the radiative power, the wave length, and water characteristics OBS [*Fairall et al.*, 1996; *Jerlov*, 1976; *Ohlmann et al.*, 2000; *Wick et al.*, 2005].

A positive net heat flux, Q_0, is defined in the positive direction of the z–axis (upwards from the interface). Q_S can be either positive or negative whereas Q_L and $Q_{R,LW}$ are typically positive (upwards). Q_0 is usually positive which results in a cooling of the surface, especially during nighttime resulting in a so-called cool skin at the surface [*Fairall et al.*, 1996; *Soloviev and Schlussel*, 1994]. The annual mean is in the range of $40 < Q_0 < 230\ Wm^{-2}$ [*Stewart*, 2008]. The shortwave radiation can especially on days without clouds, depending on the vertical distribution of the radiative absorption, influence the buoyancy flux and thereby the cool skin. The heat flux condition in the present work represents a situation with an even vertical distribution of the absorption of $Q_{R,SW}$. This condition includes the case with limited $Q_{R,SW}$ as during night time. Note also that the buoyancy flux in the atmospheric boundary layer consists of the sensible and latent heat fluxes only, which implies that the buoyancy fluxes above and below the surface are different.

1.4 Gas transfer velocity

Equation (1) is difficult to use since it is difficult to measure the gas concentration gradient in the very thin diffusive boundary layer, which has thickness δ in the order of 1 mm or less. For estimations of the air-water gas exchange, equation (1) is therefore often restated into

$$F_g = k_g(C_{wb} - \vartheta C_{\mathrm{as}}), \quad (4)$$

in order to be able to use the more easily measured bulk and air gas-concentrations instead. Here k_g is the gas transfer velocity, C_{wb} is the gas concentration in the water under the diffusive boundary layer, C_{as} is the gas concentration in the air at the water surface, and ϑ is the dimensionless Ostwald solubility coefficient (Figure 5). Even though it is easier to use C_{wb} and C_{as} instead of measuring the concentration gradient, it is now instead a challenge to estimate k_g.

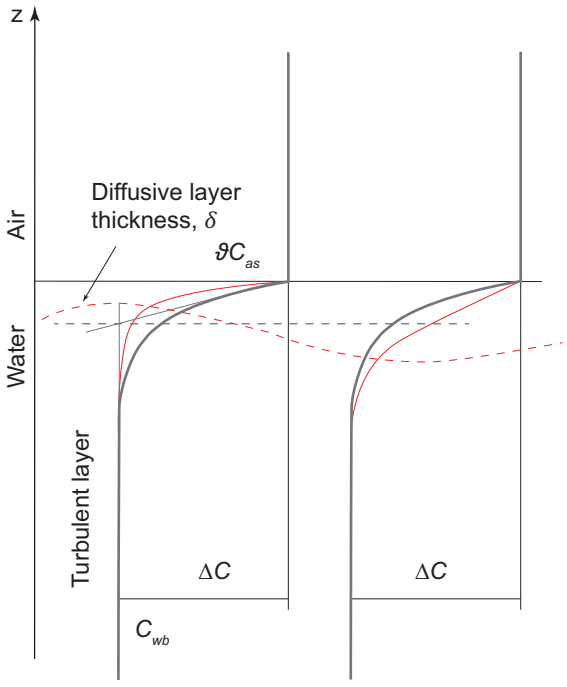

Figure 5. A schematic snapshot of the gas concentration at two different locations for a gas with a gas-flux that is controlled by the water side. The gas concentration gradients are assumed to be small in the air. The momentary gas concentration, C, and the diffusive boundary layer thickness, δ, are given in red while the mean quantities are given in grey. C_{wb} is the bulk gas-concentration in the water and C_{as} is the surface gas-concentration in the air. ϑ is the dimensionless Ostwald solubility coefficient. The water-side gas concentration gradient $\partial C/\partial z$ varies due to the varying diffusive boundary layer thickness.

In sections 1.4.1-1.4.4 four commonly used parameterizations of estimating k_g, are described, i.e., (1) based on wind speed, (2) based on surface heat flux, (3) based on rate of turbulent kinetic energy dissipation, and (4) based on surface flow divergence. All these parameterizations have a term that takes the influence of the molecular diffusivity and the abundance of surfactants at the surface into account. This influence is therefore generally discussed in section 1.4.5. Although there are other processes that influence the gas-exchange, such as white capping, sea spray, bubbles, rain, these are not taken into account in this work since white capping, sea spray, and bubbles from waves are not present during low wind conditions, and ebullition is not controlled by the surface diffusive boundary, and rain is difficult to study in DNS.

1.4.1 Estimations of k_g based on wind speed

There has been many attempts to estimate k_g based on the wind speed 10 meters above the surface, referred to as U_{10} [e.g., *Bade*, 2009; *Wanninkhof et al.*, 2009]. Two parameterizations often used are

$$k_{g,CC1998,600} = 0.215U_{10}^{1.7} + 2.07, \quad (5)$$

presented by *Cole and Caraco* [1998] for inland waters, and

$$k_{g,W2009,660} = 0.1U_{10} + 0.064U_{10}^2 + 0.011U_{10}^3 + 3, \quad (6)$$

presented by *Wanninkhof et al.* [2009] for ocean conditions. Here the transfer velocity is given in ($cm\ h^{-1}$) and the wind speed is given in (ms^{-1}). It can be seen that both these equations have constants implying that there is a gas flux also for zero-wind conditions. This gas flux (and gas transfer velocity) must then be due to processes enhanced by other means than wind speed, e.g., buoyancy flux. This is of course problematic since the variation in e.g., the buoyancy flux is not be described in these equations.

Equations (5) and (6) are given for Schmidt numbers $Sc = 600$ and 660 representing CO_2 at 20 °C in freshwater and seawater respectively. Here $Sc = \nu/D$ express the ratio of the kinematic viscosity ν and molecular diffusivity. The relation between two transfer velocities with different gas-water properties are generally expressed via their different Schmidt numbers as

$$k_{g,Sc_1} = k_{g,Sc_2}\left(\frac{Sc_1}{Sc_2}\right)^{-n}, \quad (7)$$

where n is an exponent that depends on the surface characteristics. The exponent is usually between $1/2$ and $2/3$ and represents the Schmidt number dependency and thereby the molecular diffusivity dependency on the transfer velocity.

1.4.2 Estimations of k_g based on surface heat flux

The heat transfer velocity, κ_{heat}, and an expression for the conversion between heat and gas through their Sc and Prandtl number, Pr, have been used [e.g., *Frew et al.*, 2004; *Garbe et al.*, 2003; *Haussecker et al.*, 1998] to estimate the gas transfer velocity as

$$k_{g,heat} = A_{heat}\kappa_{heat}\left[\frac{Sc}{Pr}\right]^{-n}, \kappa_{heat} = \frac{Q_0}{\rho c_p \Delta T}. \quad (8)$$

Here $Pr = \nu/\alpha$ is the Schmidt number for heat using the thermal diffusivity α instead of the molecular diffusivity used in Sc. A_{heat} is a transfer velocity constant for the parameterization based on heat flux where c_p is the specific heat capacity, and ΔT is the surface skin-bulk temperature difference across the thermal boundary layer. Equation (8) is based on the assumption that the thermal diffusive boundary layer is controlled by the same processes as the gas diffusive boundary layers. There are, however, three main differences: (i) Heat influences the buoyancy and thereby the turbulent motions below the surface, (ii) the surface boundary conditions for gas and heat differs because the transport of gas is controlled by the water side and heat by the air side, and (iii) the diffusivities can differ by orders of magnitude with $Pr = \mathcal{O}(10^0)$ and $Sc = \mathcal{O}(10^2)$ depending on which gas it is. In spite of these differences, e.g., *Jahne et al.* [1989] have shown a good agreement for oxygen ($Sc = \mathcal{O}(10^2)$) between directly measured transfer velocities and transfer velocities extrapolated from heat transfer velocities.

1.4.3 Estimations of k_g based on dissipation

The parameterization using the rate of turbulent kinetic energy dissipation is based on the theoretical framework of the eddy cell model [*Fortescue and Pearson*, 1967] but with the assumption that it rather is the small scale dissipative eddies than the large scale eddies that are the main transportation agents [*Banerjee et al.*, 1968; *Lamont and Scott*, 1970]. This assumption and the assumption that the turbulence can be described with a standard turbulence spectrum yields the gas transfer velocity as

$$k_{g,diss} = A_{diss}(\varepsilon\nu)^{1/4}Sc^{-n}\,. \tag{9}$$

Here A_{diss} is a transfer velocity constant for the dissipation parameterization and ε is the rate of kinetic energy dissipation. *Lamont and Scott* [1970] found the appropriate values to be $n = 1/2$ and $2/3$ for free fluid and solid surfaces respectively. In spite of some problems with the assumptions during natural conditions, the dissipation parameterization has performed well in many cases e.g., Paper IV, *Zappa et al.* [2003], and *Zappa et al.* [2007].

1.4.4 Estimations of k_g based on surface flow divergence

The parameterization using the horizontal flow divergence, $\gamma = \partial u/\partial x + \partial v/\partial y$, at the surface is given by

$$k_{g,div} = A_{div}(\gamma_{rms}\nu)^{1/2}Sc^{-n} \tag{10}$$

where γ_{rms} is the root-mean-square, rms, of the surface flow divergence and u and v are the horizontal velocities in the x- and y-directions at the surface. A_{div} is a transfer velocity constant for the parameterization based on divergence. The parameterization has been used in many studies [e.g., *Banerjee et al.*, 2004; *Calmet and Magnaudet*, 1998; *McKenna and McGillis*, 2004] and theoretically derived by e.g., *Ledwell* [1984].

1.4.5 Influence of surfactants

Surfactants are surface-active chemical agents that generally reduce gas exchange [e.g., *Bade*, 2009; *McKenna and McGillis*, 2004; *Wanninkhof et al.*, 2009]. They are almost always present in natural waters and occasionally the amount of surfactants even forms a surface film and then requires an extra layer to represent the surfactants when estimating the gas-exchange. Also in smaller abundances, which is the usual situation, they act to change the hydrodynamic conditions of the air-water interface [*McKenna and McGillis*, 2004]. The flow at the surface, including eddies, redistributes the surfactant concentration and makes it patchy. A surfactant lowers the surface tension, and since the surfactant concentration now is patchy, the surface tension will vary over the surface. A varying surface tension results in elastic forces that attenuate the turbulent eddies. This attenuation influences the gas exchange, in particular for the gases with thin diffusive boundary layers, i.e. those with high Schmidt numbers. The surfactant influence on the gas-flux and its attenuation can be discussed in the light of the theoretical work of *Ledwell* [1984] where the influence of molecular diffusivity on the gas transfer velocity is studied and compared for both slip and no-slip boundary conditions. This gives Schmidt number exponents $n = 1/2$ for a clean surface and $2/3$ for a surface with surfactants, if a clean surface is represented by a slip boundary condition (no attenuation of the horizontal components of the surface flow), and a

surface with a large abundance of surfactants is represented by a no-slip boundary condition (horizontal components of the surface flow is zero).

2 METHODS

2.1 Direct numerical simulations

Paper I-III use direct numerical simulations, DNS, to study how the turbulence and the heat- and gas-transports depend on different flow conditions. The gas is modeled as a passive scalar which can be seen as an inert gas. The flow conditions are varied via (i) different surface boundary conditions for the velocity (including shear and surfactants) and the temperature (surface heat flux), (ii) different depths, and (iii) different molecular diffusivities for the scalar.

The computational domain can schematically be seen in Figure 6. This schematic is in general valid for the Papers I-III. However, the horizontal plane in Paper I-II is quadratic since all the boundary conditions are identical in the spanwise and streamwise directions in these papers (no surface shear-stress). Furthermore, the y- and z-directions are defined in the vertical and the spanwise directions in Paper II.

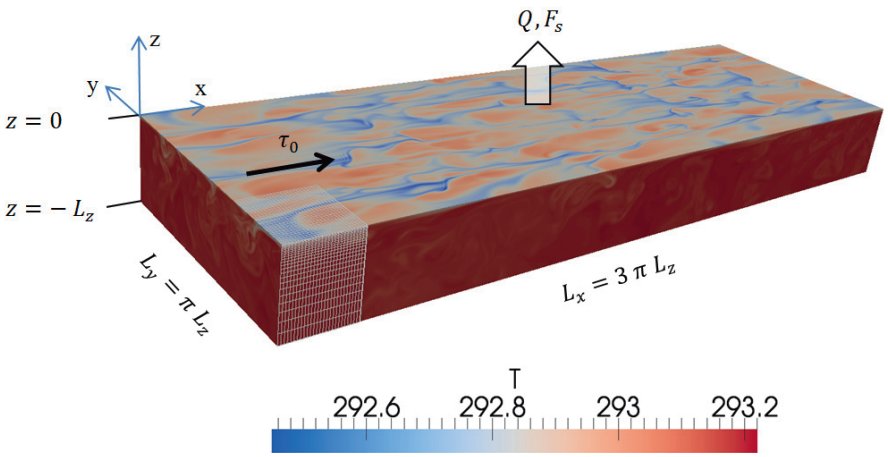

Figure 6. Computational domain for the cases with combined buoyancy and shear stress forcing. The domain size is given by $L_z = 0.1204\ m$, $L_x = 3\pi L_z$ and $L_y = \pi L_z$ in the depth, streamwise, and spanwise direction respectively. The surface is subject to a constant outward-going heat flux, Q_0, and a constant scalar concentration, S_0, while the bottom is subject to zero flux boundary conditions. The velocity boundary conditions are either slip, no-slip or constant shear stress, τ_0, at the surface boundary and slip at the bottom boundary. Periodic (cyclic) boundary conditions are used for all variables in the horizontal (x- and y-) directions. The temperature field is a snapshot from case 240B ($Re_* = 240$ with buoyancy, see section 3). (Redrawn from Figure 1 in Paper III).

DNS imply that there is no turbulence model that models or creates turbulence in the computation. The turbulence is instead "naturally" invoked due to flow instabilities that arise due to the flow forcing. The DNS method is used in order to be able to study the actual turbulence and its influence on the gas exchange by solving the small-scale turbulent motions instead of using a turbulence model. The forcing is in Paper I-III either natural convection (buoyancy) or surface shear stress or a combination of both. The lack of a turbulence model sets very high requirements on the computational mesh resolution since all the fluid motions and eddies must be resolved all the way down to the sizes where the turbulence dissipates to heat. An extensive mesh resolution and domain aspect-ratio study was therefore performed in Paper I. The resulting mesh resolution for Paper I and III can schematically be seen in the front corner of the domain in Figure 6. Here only every fourth grid line are plotted since the mesh is very fine and the grid lines otherwise would be difficult to see. The mesh is equidistant in the horizontal plane, and in Paper I and III densified towards the surface. In Paper II the mesh is densified towards both the surface and bottom. The vertical mesh spacing close to the surface is, though, the same for the meshes used in Paper I-III.

In Paper I and III a finite-volume method is used whereas a pseudo-spectral method is used in Paper II. Please also refer to Paper I-III where these methods as well as the space and time discretizations are discussed in more detail.

In all the DNS-papers (I-III) the Navier-Stokes equations

$$\frac{\partial \mathbf{U}}{\partial t} + \mathbf{U} \cdot \nabla \mathbf{U} = -\nabla \Pi + \nu \nabla^2 \mathbf{U} + \beta g\,(T - T_0)\mathbf{k} \tag{11}$$

and

$$\nabla \cdot \mathbf{U} = 0 \tag{12}$$

using the Boussinesq approximation are solved in conjunction with the transport equation

$$\frac{\partial T}{\partial t} + \mathbf{U} \cdot \nabla T = \alpha \nabla^2 T + \phi_T \tag{13}$$

for the temperature T. In Paper I and III a transport equation

$$\frac{\partial S}{\partial t} + \mathbf{U} \cdot \nabla \mathrm{S} = D \nabla^2 S + \phi_s \tag{14}$$

for a passive scalar S is solved as well. Here $\mathbf{U}=(U, V, W)$ is the fluid velocity where the components are given in x-, y-, and z-directions respectively and t is the time. $\Pi = p/\rho_0 + gz$, p is the pressure, ρ_0 is a reference density, g is the acceleration of gravity, $\mathbf{k}$ is a unit vector in the vertical direction, ν is the kinematic viscosity, $\beta = (-1/\rho_0)(\partial\rho/\partial T)|_0$ is the thermal expansion coefficient, ρ is the density, T is the temperature, T_0 is a reference temperature, α is the thermal diffusivity, S is the scalar concentration, and D is the molecular diffusivity of the scalar in water. In order to sustain a constant mean temperature in the domain an evenly distributed heat source ϕ_T is added to equation (13) to balance the heat flux through the surface. Similarly an evenly distributed pressure gradient (not shown) is added to equation (11) in the direction opposite to the surface shear stress cases in Paper III. The scalar source $\phi_s = F_{so}/L_z$ is used to impose the scalar flux through the surface and F_{so} is the area-

averaged mean scalar flux once steady-state is achieved. In the following, $(u, v, w), \theta$, and s are used to represent the fluctuating parts of $(U, V, W), T$, and S respectively.

The surface boundary is flat, assuming that the surface deflection is negligible. The surface boundary condition for the vertical velocity is therefore $W = 0$ for all cases. The boundary conditions for the horizontal velocities are for the pure convection driven cases without surfactants (Paper I) either a slip ($\partial U/\partial z = \partial V/\partial z = 0$) or a no-slip ($U = V = 0$) boundary condition. In Paper II the surfactant boundary conditions for the horizontal velocities are $\partial U/\partial z = \xi\, \partial\sigma/\partial x$ and $\partial V/\partial z = \xi\, \partial\sigma/\partial y$ where $\xi = \sigma_0 L_z/\nu\rho\alpha$. The surface tension σ is a function of the surfactant concentration Γ and is linearized around the initial surface-tension σ_0. For the cases in Paper III driven by pure surface shear-stress or by a combination of natural convection and surface shear-stress there is a slip boundary condition in the y-direction and a shear-stress boundary condition in the x-direction ($\partial U/\partial z = \tau_0/\nu\rho$). Here τ_0 is the surface shear stress. The bottom boundary is assumed to be stress-free and is modelled with a slip boundary condition for all cases.

The surface boundary condition for the temperature is $\partial T/\partial z = Q_0/\lambda$ assuming a constant surface heat flux, Q_0 [*Soloviev and Schlussel*, 1994]. Here λ is the thermal conductivity. The surface boundary condition for the scalar is a constant scalar concentration $S = S_0$ assuming that the air-water gas exchange is controlled by the water-side [Jahne and Haussecker, 1998]. The bottom boundary conditions for the temperature and scalar are $\partial T/\partial z = \partial S/\partial z = 0$ assuming no heat or gas exchange through that boundary.

Periodic (cyclic) boundary conditions are used for all variables in the horizontal (x- and y-) directions.

2.2 Field measurements

The field measurements reported in Paper IV were performed in order to compare different methods of estimating k_g in the field. These methods comprise (i) flux chamber measurements, (ii) parameterization of k_g as a function of the rate of turbulent kinetic energy dissipation, and (iii) parameterization of k_g as a function of the surface divergence. Here the surface divergence was estimated via particle image velocimetry (PIV) of the surface temperature structures recorded by IR imagery. In addition to these parameterizations a number of environmental parameters were measured in an attempt to find other methods of estimating k_g. These parameters comprise e.g., bulk temperature (mean and rms), surface temperature (mean and rms), IR surface velocity mapping (mean and rms), mean IR coherent structure size, and wave height. The measurements were performed in August 17-18 2010 in Gullmarsfjord at the Bornö marine research station close to Lysekil, north-west of Gothenburg, Sweden. The measurement setup at the suspension bridge at Bornö, where the depth is about 33 m, is sketched in Figure 7. The simultaneous measurements were recorded during one diurnal cycle.

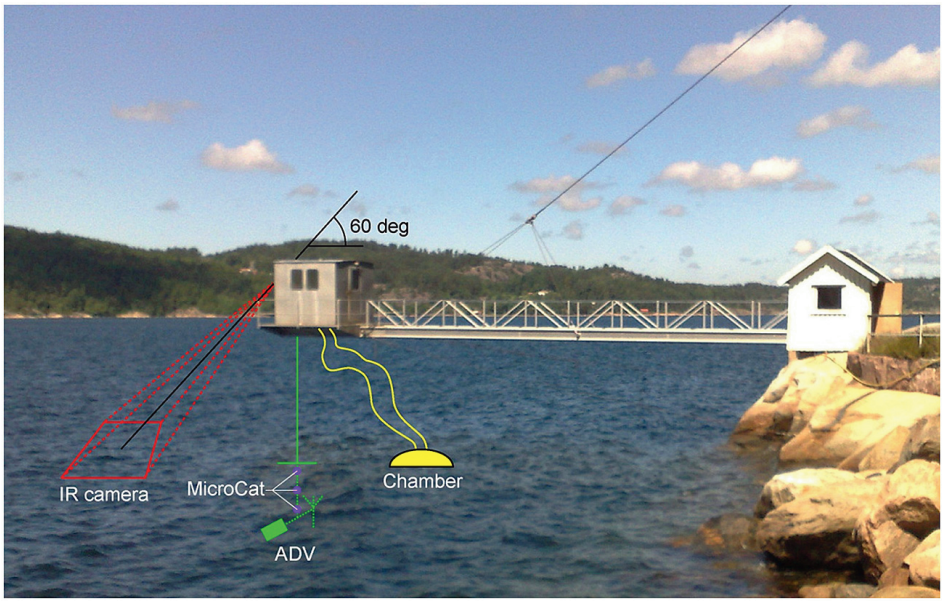

Figure 7. Illustration of the instrument setup at the Bornö suspension bridge. Three instruments were used simultaneously to measure k_g: An IR camera, an ADV, and a flux chamber with tubes for continuous measurements. (Figure 1 in Paper IV).

2.2.1 Flux chamber method

Here k_g was estimated by measurements of the gas flux across the air-water interface and the gas concentration in the water and air inside the chamber. The gas flux was estimated by measuring the concentration change dC/dt inside a round lightweight chamber that was placed at the water surface. The concentration change was then transformed into flux using the common gas law, the volume of the chamber, and the surface water area covered by the chamber. The implicit assumption is that the concentration change is caused by fluxes through the surface, and that the flux inside the chamber is similar to that outside the chamber. The concentration at the surface (ϑC_{as} in equation (4)) was estimated as the equilibrium concentration of the gas at the surface using the initial gas concentration in the chamber and Henry's law. Here, the assumption is that the gas concentration outside the chamber is equal to the initial concentration in the chamber. The bulk gas concentration in the surface water (C_{wb} in equation (4)) was measured at the start and end of each measurement period at a depth of approximately 40 cm. Although fluxes of both CO_2 and CH_4 were measured, only CH_4-fluxes were used for estimating k_g. The rationale is that there was always a significant positive net flux of CH_4 into the chamber while the fluxes of CO_2 showed more variation with both release from and uptake to the water with intermediate periods of no significant flux during the measurement period. The transfer velocity for CH_4 was transformed into k_{600} according to equation (7) with $n = 1/2$.

The edges of the chamber was submerged only 2.5 cm into the water due to the lightweight chamber construction and the chamber was attached to the bridge with

thin, slack strings enabling it to move with the water as freely as possible. This has previously been shown to be successful for chamber performance [Cole et al., 2010].

2.2.2 Dissipation rate parameterization

The rate of the turbulent kinetic energy dissipation, ε, was estimated from the turbulence spectra at approximately 0.3 m depth. The transfer velocity was then calculated with equation (9) with $A_{diss} = 0.42$ as found by *Zappa et al.* [2007]. The spectra were calculated from 3D velocity vector time series recorded by the use of acoustic doppler velocimetry (ADV) . The ADV was mounted looking upwards on a taut line hanging from the bridge. A fin on the ADV ensured that the sensor was upstream of the line (undisturbed).

2.2.3 Surface divergence parameterization via IR and PIV

It has been shown in laboratory experiments that particle image velocimetry (PIV) can be used to determine the surface divergence. *Veron et al.* [2008] extended this idea, and used infrared (IR) imagery of the ocean surface to estimate surface velocity, vorticity, and surface divergence. The idea is that the surface temperature (heat pattern) measured with an IR camera can be used as a fluid flow tracer, see Figure 8. This was in Paper IV also confirmed to be the case by comparing (directly in the IR image sequences) the motion of the bubbles and foam at the surface with the motion of the heat pattern. It should, however, be noted that thermal IR radiation has very short transmission lengths in water (order of $1 - 100\mu m$, [e.g., *Garbe*, 2001]) which means that PIV of heat-patterns estimates the velocities in the very top surface water (skin) which in turn may be different from the velocities just below the surface [*Volino and Smith*, 1999]. The use of the heat pattern as a fluid flow tracer can be problematic for certain flow conditions, e.g., pure natural convection where there can be a horizontal flow inside a more or less stationary plume as will be seen in section 3.1. That type of flow would not be detected with IR/PIV, which only recognizes the motion of temperature anomalies such as the streaks of the cold water enclosing the warm plume. This problem is decreasing for cases where there is more than pure natural convection forcing. It should also be noted that the temporal and spatial resolution of the IR imagery and the PIV must be high enough to estimate the surface divergence properly.

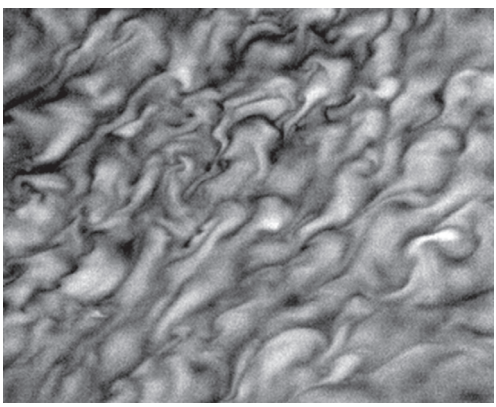

Figure 8. Example of a temperature field from an IR image. The average field of view is 95×88 *cm. (Part of Figure 4 in Paper IV).*

3 CONTRIBUTIONS

In Paper I-IV a vast amount of results are presented, discussions are performed, and conclusions are drawn. In this section of the thesis an effort to synthesize all this in major contributions has been made. In order to do so a new numbering system for all the numerical cases could have been presented. This could, however, also lead to misinterpretations since all the cases are more thoroughly described in each paper than in this synthetization of the results. Hence the cases were chosen to be presented here with the same labeling as in the papers enclosed.

The cases in Paper I are named with (i) a letter s for $s$lip or n for no-slip surface velocity boundary conditions, (ii) a number describing the computational domain aspect ratio, (iii) a letter B or F for the Base case or a Fine mesh resolution, (iv) and a letter S or D for a Deep or a Shallow domain or L or H for a Low or High surface heat flux. The case name $s2BH$ represents i.e., a case with a slip surface velocity boundary condition, a domain aspect ratio of 2, a base case mesh resolution, and a high surface heat flux.

The wind forcing is in Paper III modeled as a fixed shear stress $\tau_0 = \rho u_*^2$. The cases are named with (i) a number for the shear-based Reynolds number for $Re_* = u_* L_z/\nu$, which describes the ratio between inertial and viscous forces, and (ii) a letter B for Buoyancy or letters NB for No-Buoyancy. In the no-buoyancy cases the gravitational acceleration was set to zero, so the temperature acted as a passive tracer only. The domain aspect ratio, domain depth, and the mesh resolution was the same for all cases. Furthermore, the case $0B$ in Paper III is identical with the case $s2B$ in Paper I.

In the plots to come, $\bar{\xi}$ and $\langle \xi \rangle$ denote volume and horizontal area ensemble mean of an arbitrary variable ξ, respectively.

3.1 General gas-exchange characteristics for buoyancy driven flow

In Figure 9 a snapshot of case $0B$ (slip boundary condition and base case heat flux and mesh resolution) is presented in order to give an introduction to many of the results presented later in this section.

The surface heat flux cools the surface water and thereby makes it denser. Due to instabilities this denser water then starts to descend in thin plumes sketched as blue arrows. The descending plumes set up a horizontal flow sketched with yellow arrows and an ascending flow of warmer water between the descending plumes. The descending plumes are typically much thinner than the ascending warm water. The horizontal and ascending flow typically stretch and squeeze the diffusive boundary layer and thereby make it thinner. The patches with thin diffusive layer thicknesses are here visible as “islands” penetrating the mean thickness, separated with trenches of limited vertical diffusive transport.

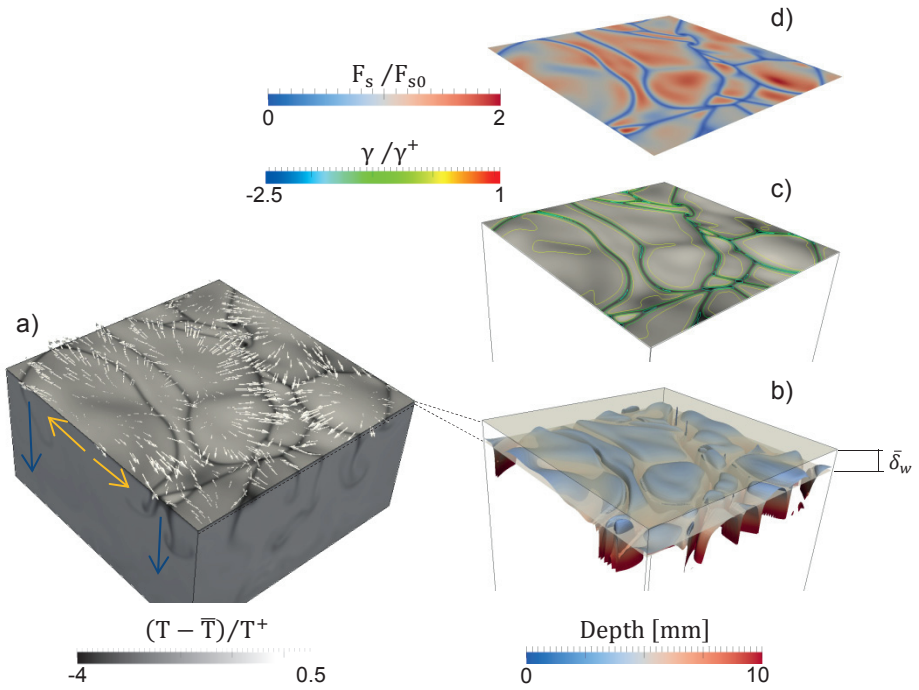

Figure 9. Snapshot for the case 0B (pure buoyancy forcing with slip surface boundary condition). (a) The normalized temperature field $(T - \overline{T})/T^+$ and the surface water velocities. Blue and yellow arrows schematically represent the descending plumes and the horizontal flow close to the surface. (b) The mean and momentary diffusive boundary layer thickness, $\bar{\delta}$ and δ, where the thickness is defined as where 5% of the total vertical transport is diffusive. The iso-surface of the momentary diffusive layer is colored by the actual layer thickness where colder color means smaller thicknesses. The vertical dimension in the plot is scaled by five for better visibility. (c) The temperature field and contours of the normalized horizontal flow divergence, γ/γ^+, at the surface. (d) The surface-normal scalar transport, F_s/F_{s0}, for $Sc = 7$ across the surface.

Figure 5 sketches a varying diffusive layer depth similar to what would be the results if Figure 9b was sliced with a vertical plane. It is seen in Figure 5 that a small layer depth results in a higher concentration gradient, which in turn results in an increased surface-normal diffusive transport (Figure 9d). This increased gas flux can now in Figure 9d be seen to coincide with the "islands" with thin boundary layer thickness in Figure 9b. This is the reason for the good correlation between the temperature, and horizontal flow divergence fields that can be seen in Figures 9a,c and eventually also between the momentary diffusive layer depth and surface-normal scalar flux seen in Figures 9b,d.

3.2 Scaling

Nondimensional numbers and scales for e.g., length, time, velocity, temperature, and scalar concentration can be used as tools to facilitate the understanding of which processes and scales that are important in determining the transfer velocity. Paper I presents scales that are appropriate for the analysis of flows driven by pure natural convection (buoyancy forcing). These scales, presented in Table 1, are divided in inner

and outer scales. The inner scales are based on the assumption that it is the processes in the vicinity of the surface that control the gas transfer whereas the outer scales are based on the assumption that it is the whole domain (surface mixed layer) that controls the gas transfer. The inner scales will be used to discuss the results in sections 3.3 and 3.4 since these scales were found in Paper I to best scale the processes of importance for the gas transfer velocity.

Table 1 Scaling schemes

Scheme	Length, L	Velocity, W	Time, t	Temp., T	Scalar, s	Div., γ
Inner ($^+$)	$Sc^{n-1}\left(\frac{\nu^3}{B}\right)^{1/4}$	$Sc^{-n}(B\nu)^{1/4}$	$Sc^{2n-1}\left(\frac{B}{\nu}\right)^{-1/2}$	$Q_0 Pr^n (B\nu)^{-1/4}$	$F_{s0} Sc^n (B\nu)^{-1/4}$	$1/t^+$
Outer (*)	L_z	$(BL^*)^{1/3}$	$\left(\frac{B}{L^{*2}}\right)^{-1/3}$	$Q_0 (BL^*)^{-1/3}$	$F_{s0}(BL^*)^{-1/3}$	$1/t^*$

The mixing layer depth is in these simulations assumed to be the domain depth L_z.

It is more intriguing to find suitable scales for the cases with combined forcing. A flow dominated by buoyancy forcing should use the above scales while a flow dominated by shear forcing should use the shear scales presented in Paper III. These scales and the transition from one set of scales to the other are discussed in more detail in Paper III. Furthermore, dimensional analysis in paper III shows that the gas transfer velocity for a case with combined forcing from both buoyancy and shear stress can be expressed in non-dimensional relationships according to

$$\frac{k}{u_*} = \psi(Sc, Pr, Re_*, Ri). \tag{15}$$

where Sc and Pr have been defined above. The Reynolds number

$$Re_* = \frac{u_* H}{\nu} \tag{16}$$

based on the friction velocity, $u_* = \sqrt{\tau_0/\rho}$, represents the ratio between the inertial and the viscous forces. Here, H, is the depth of the surface mixed-layer (generally considered as a quasi-homogenous region in the upper ocean characterized of little variation in density and temperature with depth [*Kara et al.*, 2000]). It is here assumed to be represented by the computational domain depth L_z. The validity of this assumption is discussed in section 3.3. The fourth variable is a Richardson number defined as

$$Ri = \frac{B\nu}{u_*^4}, \tag{17}$$

representing the ratio between the buoyancy and shear forcing. Here $B = \beta g Q_0/\rho c_p$ is the buoyancy flux just below the surface. Ri will be used in section 3.5 as a measure of the transition from buoyancy- to shear-dominated gas transfer.

3.3 Influence of natural convective forcing and surface mixed layer thickness on gas transfer velocity

The momentary temperature fields at the surface for three different surface heat fluxes are given in Figure 10. The upper row (Figures 10a-c) shows the temperature variation in dimensional units (°C) whereas the temperature has been normalized with the inner temperature scale T^+ in the lower row (Figures 10d-f). It can in be seen that the flow features typically become smaller for stronger natural convection forcing. The temperature variation is increasing at the same time (i.e., a higher surface heat flux gives higher buoyancy flux which results in smaller flow features and larger temperature variation). The larger temperature variation is seen as an increasing contrast in Figures 10a to 10c The strength and validation of the scaling practice is shown in Figures 10d-f where it is seen that the temperature variation scales well with the inner temperature scale $T^+ \propto Q_0^{3/4}$ (approximately the same contrast, which here represents the normalized temperature variation).

Statistics for temperature and scalar concentrations for these cases with a heat flux variation as well as for the cases with a depth variation are presented in Figure 11. It shows the horizontally averaged rms and mean values of the temperature and scalar concentrations. The convective inner scales for length, temperature, and scalar concentration have been used for the normalization. It can be seen that these scales collapse the results for both the temperature and scalar concentration very well. This is interesting since all of the inner scales (T^+, s^+, and L^+) that are used in Figure 11, are functions of either the heat or scalar flux, and Sc, n, ν, and B but not the vertical dimension of the computational domain. This is also manifested in Figure 9 in Paper I where the transfer velocity dependence of the buoyancy flux and domain depth is presented. There is a clear transfer velocity dependence of the buoyancy flux $k \propto B^{1/4}$ but only a very limited dependence of the domain depth. Furthermore, it is shown in Paper I that outer scaling, that includes the domain depth for buoyancy driven flows, does not scale the near-surface processes as apt as the inner scaling. This implies that, (i) for large enough depths, the surface mixed layer thickness does not influence the gas transfer velocity, (ii) the gas transfer velocity is a function of the buoyancy flux, and (iii) the domain depth in the simulations is large enough to model the processes in the surface mixed layer for near-surface processes as the interfacial gas-flux processes.

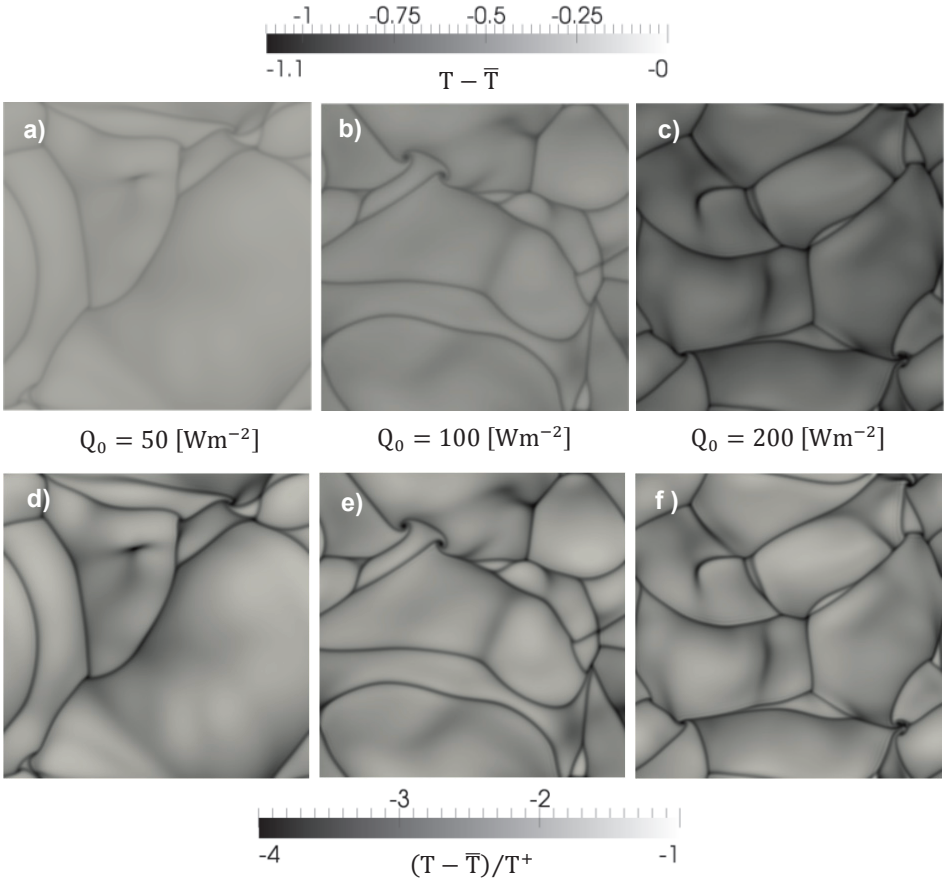

Figure 10. Momentary temperature fields at the surface for three different surface heat fluxes where $Q_0 = 100\ Wm^{-2}$ is the base case heat flux. The upper row (a-c) shows the temperature $T - \overline{T}$ and the lower row (d-f) shows the normalized temperature $(T - \overline{T})/T^+$ with a common scale. $\overline{T}$ is the domain mean temperature and $T^+ = Q_0 Pr^n (B\nu)^{-1/4}$ is the convective inner scale. These cases are presented as s2BL, s2B, and s2BH in Paper I.

Furthermore, Figure 11 shows that T_{rms} and S_{rms} differ close to the surface due to the two different surface boundary conditions for the temperature (constant heat flux i.e. constant temperature gradient) and scalar (constant concentration). Nevertheless, the figure also shows that the mean gradients are very similar. This is interesting from a gas-transfer-velocity point of view, since the mean temperature magnitudes, as a function of the depth, are used in the parameterization based on the heat flux (equation (8)). This high similarity therefore gives reason to believe that the parameterization based on the heat flux will work, as discussed further in Section 3.7.

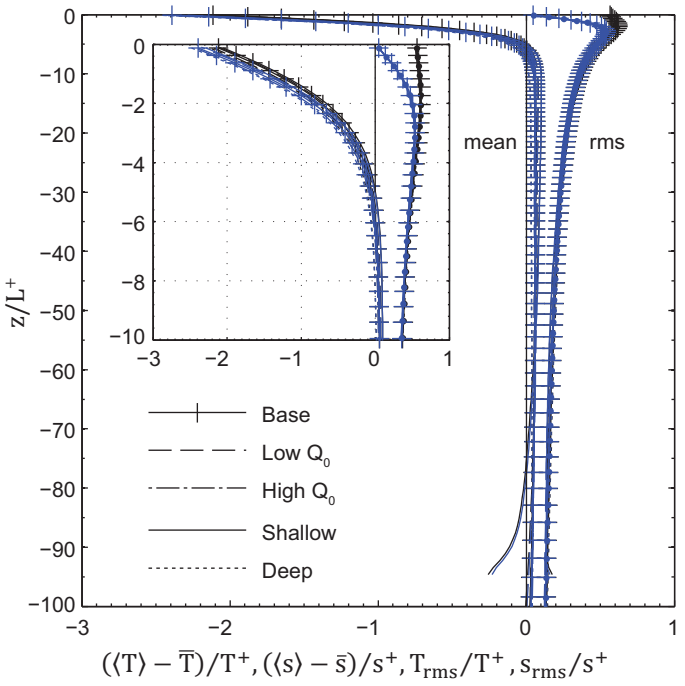

Figure 11. Mean and rms temperature (black) and scalar concentration (blue) normalized with convective inner scales, T^+ and s^+. The depth is normalized with L^+. The inset is a zoom of the near-surface area. The different cases are difficult to distinguish in the plot since the normalization collapse the results very well. These cases are presented as s2B, s2BL, s2BH, s2BS, and s2BD in Paper I.

3.4 Influence of gas diffusivity and surfactants on the gas transfer velocity

The influence of gas diffusivity was studied in Paper I by modeling scalars with $Sc = 7$, 150, and 600 respectively. These $Sc = \nu/D$ numbers were chosen as (i) one equivalent with the $Pr = \nu/\alpha$ number which can be seen as the Sc number for heat, (ii) one that is equal to the Sc number usually used for CO_2 in fresh water, and (iii) one in-between.

According to Ficks law given in equation (1), the diffusive gas flux depends linearly on the diffusivity. This means in general that, in order to maintain the same gas flux, the gas concentration gradient must be larger for a gas with low molecular diffusivity than for a gas with high molecular diffusivity. A larger concentration gradient can be achieved by either a thinner boundary layer or a larger concentration difference across the layer. It is shown in Figures 12a-b to be both. Here both the diffusive boundary layer thickness, δ_{600}, is thinner and the concentration difference is larger for a scalar with $Sc = 600$ than for a scalar with $Sc = 150$ and even more so for $Sc = 7$. This tendency can be seen to be amplified for the no-slip condition (Figure 12b) compared to the slip condition (Figure 12a). Both the changing boundary-thickness and concentration-difference scale well with L^+ and s^+ with $n = 1/2$ and $n = 2/3$ for slip and no-slip, respectively (Figures 12c-d).

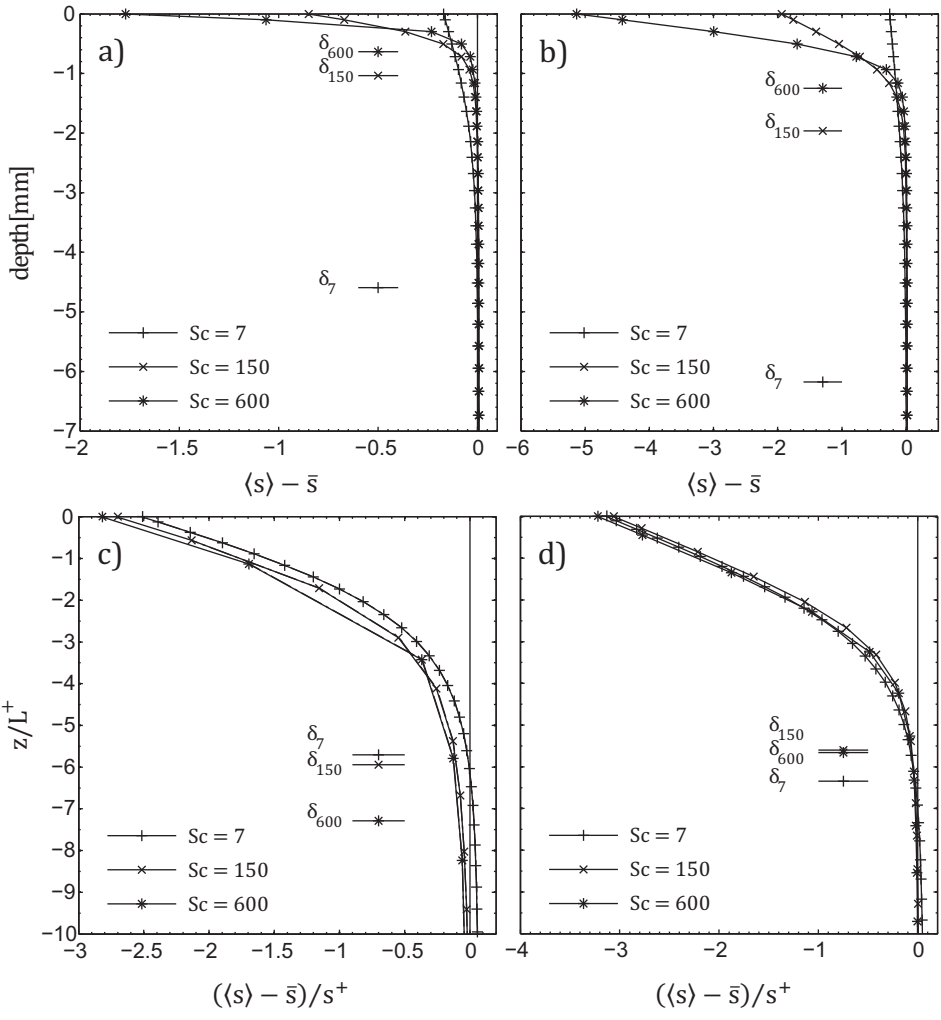

Figure 12. Mean scalar concentration for slip and no-slip boundary conditions. Concentrations and the sublayer thicknesses, δ, are given for scalars with Sc numbers equal to 7, 150 and 600. (a) Slip boundary conditions. The results for s2B (base case mesh resolution) are presented with a full line while the results for s2F (fine horizontal mesh resolution) are presented with a dash-dotted line. The results are very similar and therefore the full and dash-dotted lines are difficult to distinguish in the plot. (b) No-slip boundary conditions, n2B. (c-d) as (a-b) but scaled with inner scales L^+ and s^+ with $n = 1/2$ and $n = 2/3$ for slip and no-slip boundary conditions, respectively. (Part of Figure 13 in Paper I)

A higher *Sc* number (i.e. lower diffusivity) requires in general a finer mesh resolution in order to be fully resolved. The effect of a too coarse mesh can be seen (Figure 12 in Paper I) as oscillations in the concentration for the higher *Sc* numbers. It is, however, argued with support from the mesh sensitivity analysis, also performed in Paper I, that the uncertainty in the results due to too coarse mesh resolution is acceptable for the averaged flow quantities of interest for the gas-exchange evaluation. It can e.g., be seen

in Figure 12a that case $s2B$ and $s2F$ give virtually the same scalar mean concentration although $s2F$ has a finer mesh resolution than the base case $s2B$.

The influence of the abundance of surfactants for flows driven by natural convection is studied in Paper II. The results show that the surfactant influence depends both on the mean surfactant abundance at the surface and on the turbulent conditions in the flow underneath the surface. Furthermore, it is possible to estimate this influence by a turbulence-surfactant parameter β_E expressing the ratio of elastic to inertial forces. By increasing the surfactant abundance it is also found that there eventually is a saturated surfactant abundance. At this abundance, the studied flow parameters (i.e. rms velocity, rms and mean temperature, dissipation and mean absolute divergence) are not affected further for an increased abundance. It is further shown that there is a smooth transition for these flow parameters from the clean to the saturated surfactant condition (Figure 4 in Paper I).

In Paper I the results from Paper II are compared to the results with a slip and a no-slip boundary condition. This is done in order to find out if the less resource-demanding no-slip boundary condition can be used to study flow conditions with surfactants. It is shown that the results for the no-slip boundary conditions are very similar to the saturated surfactant case except for the rms horizontal velocity close to the surface. This is zero for no-slip and non-zero for surfactant boundary conditions. At a first glance, it is surprising that the flow divergence (which is important for gas-exchange) can have a similar behavior for the two different boundary conditions although the rms horizontal velocities differ close to the surface. The similarity in flow divergence can be explained by a decomposition of the horizontal flow into a solenoidal and an irrotational component (see Figure 13) [*Hasegawa and Kasagi*, 2008]. A surfactant boundary condition mainly dampens the irrotational component, which is the dominating contributor to the horizontal flow divergence while the solenoidal component is less dampened and still contributes to the rms horizontal velocity. To summarize, it is therefore found that a slip and a no-slip boundary condition can be used to model a clean and a saturated surfactant condition, respectively, when studying gas transfer.

Figure 13. Decomposition of the interfacial velocity vector into (a) solenoidal and (b) irrotational components. (Figure 4 in Hasegawa and Kasagi [2008])

The resulting transfer velocities, k_s, for slip and no-slip boundary conditions for scalars with $Sc = 7$, $Sc = 150$, and $Sc = 600$ are shown in Figure 14. The transfer velocity decreases by a factor of approximately 3 for a no-slip (surfactant-saturated) compared to a slip (clean) boundary conditions, which matches laboratory results for gas transfer velocities for clean and contaminated surfaces [*McKenna and McGillis*,

2004]. The difference is decreasing with decreasing Sc and is approximately 1.5 for $Sc = 7$.

Furthermore, it is seen that the results for the gas transfer dependence of the Sc numbers closely follow theoretical derivations [e.g., *Ledwell*, 1984]. The DNS give $k_{Sc} = k_{600}(Sc/600)^{-n}$ with $n \approx 0.521$ and ≈ 0.668 , whilst $n = 1/2$ and $n = 2/3$ in the theoretical derivation for slip and no-slip, respectively. This is the first time to the best of our knowledge that this Sc dependency has been confirmed with DNS. The close agreement with the result of the theoretical derivation is interesting since it is based on the $w_{rms}(z)$ in the vicinity of the surface, and the assumption that $w_{rms}(z) \propto z$ for a clean surface (slip) and $w_{rms}(z) \propto z^2$ for a surface with surfactants (no-slip). This assumption is as shown in Paper I only valid for the innermost part of the diffusive boundary layer for $Sc = 7$, which in turn, implies that it actually is the processes in the very vicinity of the water surface that controls the gas exchange during natural convection.

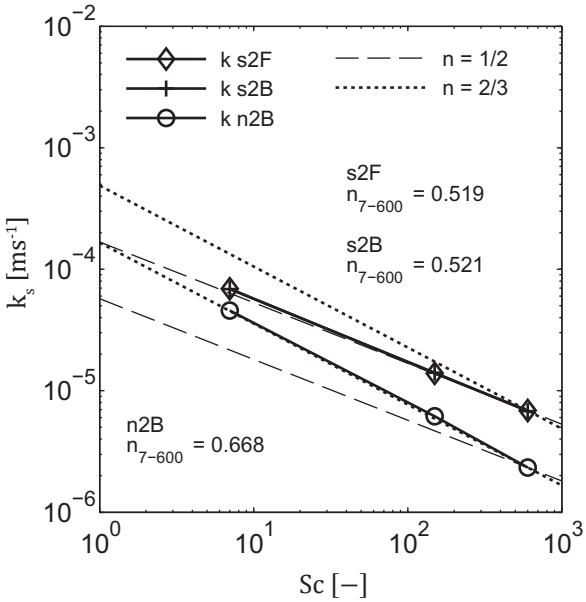

Figure 14. Scalar transfer velocity for cases s2B, s2F (both slip, clean surface) and n2B (no-slip, saturated surfactant) for three passive scalars with Schmidt number $Sc = 7$, $Sc = 150$, and $Sc = 600$, respectively. The results for the base case s2B and the case with finer mesh resolution, s2F, are difficult to distinguish since they are very similar. Dashed and dotted lines correspond to $n = 1/2$ and $n = 2/3$ and originate from $k_{s,600}$ for the slip and no-slip boundary condition case respectively.

Here the parameterization of the transfer velocity for pure natural convection

$$k_s = A_{Buoy}\,(Bv)^{1/4}\,Sc^{-n}\,, \tag{18}$$

can be presented before the results for the cases with combined buoyancy and shear-stress forcing are presented in the section to come. $A_{Buoy} = 0.4$ is a transfer velocity coefficient and $n \approx 1/2$ for slip (clean) and $n \approx 2/3$ for no-slip (saturated surfactant) boundary conditions at the surface.

3.5 Influence of combined wind and buoyancy forcing on the gas transfer velocity

One of the major contributions of this thesis is to find at which conditions the buoyancy- and wind-forcing dominate the gas transfer velocity. The results for low wind speed conditions ($U_{10} < 2ms^{-1}$) from the numerical study in Paper III are discussed in this section while the results for intermediate wind speed from the field measurements presented in Paper IV will be discussed in section 3.6.

In order to help the reader we repeat that the cases are named with (i) a number for the shear-based Reynolds number $Re_* = u_* L_z/\nu$, which describes the ratio between inertial and viscous forces, and (ii) a B for *B*uoyancy or NB for *N*o-*B*uoyancy. The case $0B$ in Paper III is identical with the case $s2B$ in Paper I.

The flow pattern for buoyancy driven flows is characterized by thin descending plumes of cold dense water, warm wider ascending plumes, and occasionally surface-normal vortices. The surface normal scalar flux follow this pattern (Figures 9a and d). Figure 15 shows snapshots of the surface normal scalar flux fields at the surface for the case $0B$ (pure convective forcing) and the cases with combined and pure shear forcing. It is seen that once the shear stress is applied to the surface (in the x-direction towards right in the figures), the pattern and vortices start to be bended and stretched and a fish-scale pattern becomes visible.

Wall-bounded flows have been shown to typically create streaky structures in the vicinity of the wall with a spanwise spacing of about $100L_*$ [e.g., *Kim and Moin*, 1989; *Kim et al.*, 1987]. Later it was shown to be valid for temperature fields and slip boundary conditions as well [e.g., *Handler et al.*, 2001]. It can now be seen that the coherent structures in the fish-scale patterns follows this *streak spacing* length scale well for cases driven by pure shear-stress ($120NB$ and $180NB$ in Figure 15). It can, however, also be seen that these coherent structures typically are finer with than without buoyancy comparing $120B$ with $120NB$ and $180B$ with $180NB$. The scalar flux variation is increasing with increasing shear forcing and the variation is higher for pure shear forcing than for combined forcing. These difference between cases with pure shear and combined forcing decrease with increasing shear-stress (increasing Re), indicating that the buoyancy forcing becomes less important. It is in the following shown that this transition in the scalar flux pattern (decreasing difference) is accompanied by transitions in many other flow characteristics and eventually the gas transfer velocity.

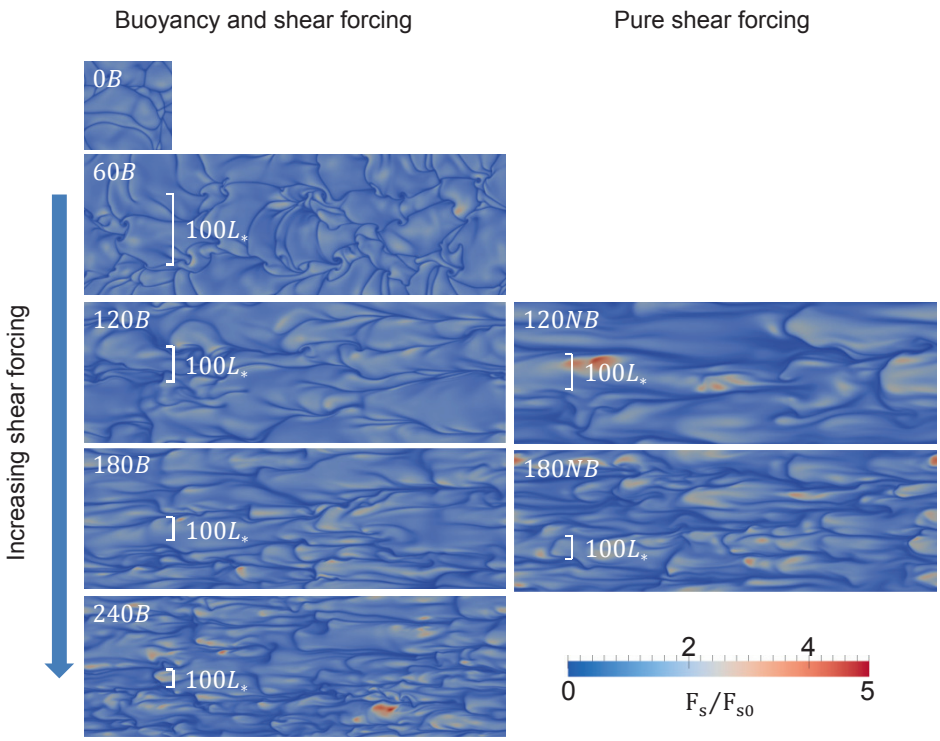

Figure 15. Normalized surface-normal scalar flux fields. The cases are named as the $Re_* = u_* v/H$ *and B for Bouyancy and NB for No-Buoyancy. The same scaling is used for all subplots. The length scale* $100L_*$*, where* $L_* = \nu/u_*$*, is indicated in the subplots for cases with* $u_* > 0$*. Case 60B is not shown in Paper III since it needs further sampling time before statistical post processing. The simulation has, however, reached its steady state condition so that a snapshot can be used as is done in this figure.*

Figure 16 shows the surface-normal scalar flux at the surface, the scalar concentration in the interior and iso-surfaces of the positive and negative streamwise vorticity Ω_x. By comparing Figure 9 with Figure 16, the transition from buoyancy to shear stress dominated flow can be seen within the interior of the flow as well. It is shown that the vorticity cores are more elongated and surface-centered for increasing shear-stress. Furthermore, it can be seen that the variation of the normalized surface-normal flux is increasing (note the different scales) with streaks of intense flux (red) as the shear stress is increased. The zoomed square shows the interplay of streamwise vorticity, scalar concentration and surface-normal scalar flux clearer. Here it is seen that water with low scalar concentration is drawn downwards (downwelling) between the vorticity-cores shifting from positive to negative in the y-direction (diagonally from the left to the right). This phenomenon is similar to the thin plumes of dense water in the case with no shear shown in Figure 9. Concurrently, areas of thin diffusive boundary-layers are formed between the vorticity-cores changing sign from negative to positive, and these areas then coincide as expected with areas of high surface-normal scalar-flux (upwelling).

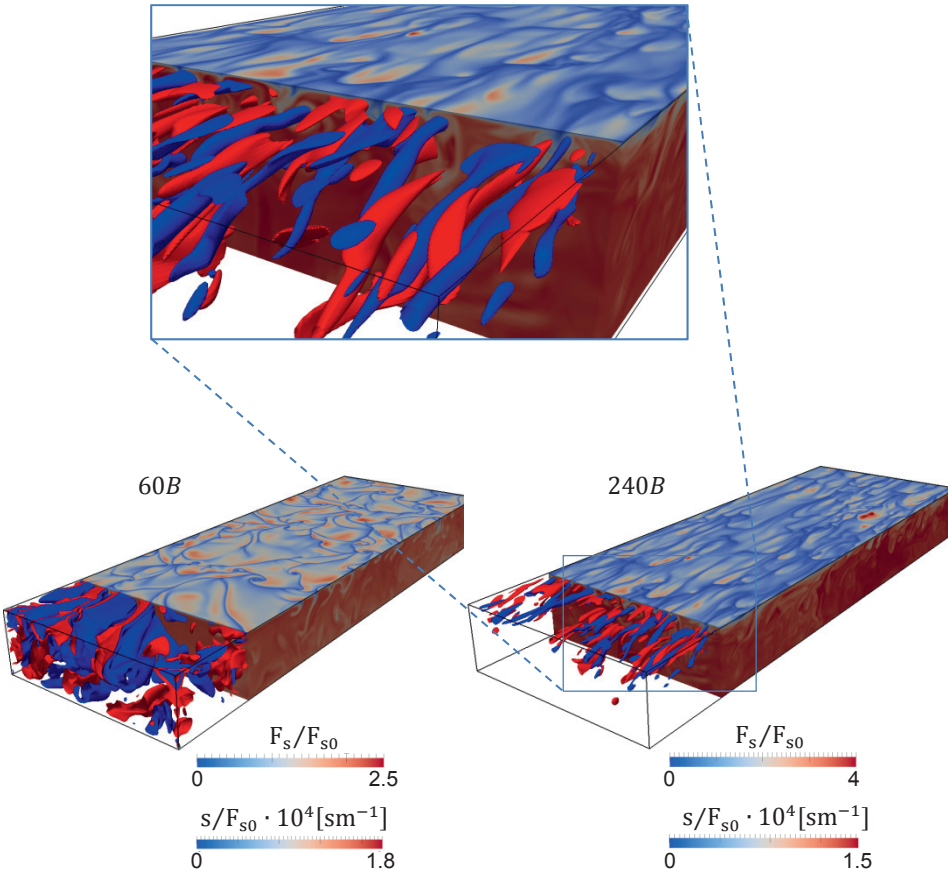

Figure 16. Snapshots for case $60B$ *(low left) and* $240B$ *(low right) and a blow-up from case* $240B$*. Surface-normal scalar flux* F_s/F_{s0} *at the surface and scalar concentration* s/F_{s0} *in the interior of the domain. Isosurfaces of normalized streamwise vorticity* $\Omega_x/(u_*^2/\nu)$ *equal* 0.25 *and* -0.25 *colored red and blue, respectively. (Figure 3 in Paper III).*

The scalar transfer velocities $k_{s,7}$ increase linearly with u_* for cases with pure shear-stress forcing (Figure 17a). These results are close to the measurements of gas transfer velocities in a wind tank [*Jahne et al.*, 1987]

$$k_{J1987} = A_{\chi J1987} u_* Sc^{-n}, A_{J1987} = 8.9^{-1}, \quad (19)$$

given in the same figure. Combined forcing gives on the other hand a more or less constant $k_{s,7}$ for low u_*, and then $k_{s,7}$ seems to connect to the linear trend as u_* increases. Another way of expressing this can be seen in Figure 17b where $k_{s,7}/u_*$ as a function of Ri is presented following equation (15). Here $k_{s,7}/u_*$ is declining down to a limiting magnitude for decreasing Ri. This limiting magnitude is set by the no-buoyancy cases. A Richardson number $Ri \approx 0.004$ is found to express the conditions when the scalar transfer starts to change from being dominated by buoyancy forcing to shear-stress forcing which is relevant for determining the buoyancy influence [e.g., *Macintyre et al.*, 2002; *Read et al.*, 2012; *Rutgersson and Smedman*, 2010].

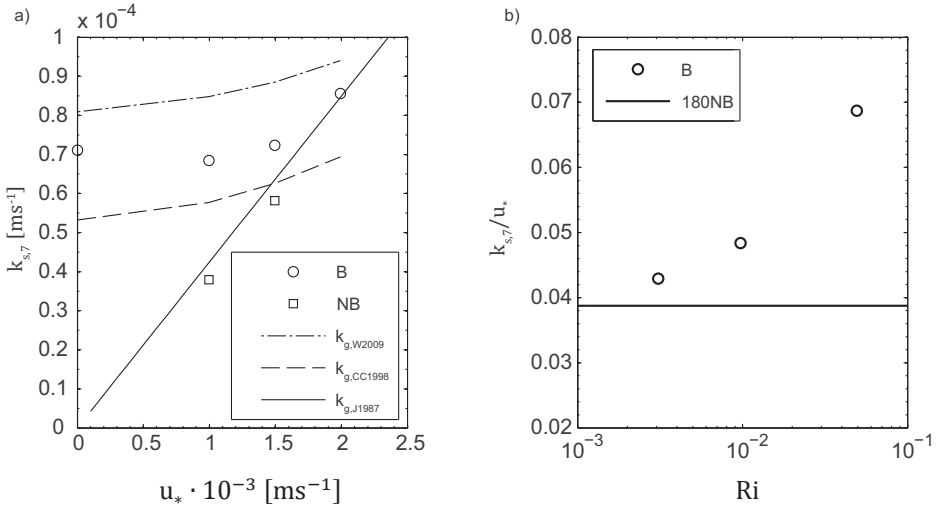

Figure 17. (a) The scalar transfer velocity $k_{s,Sc} = F_{s,Sc}/\Delta s_{Sc}$ *. Circles denote cases with buoyancy and squares denote no-buoyancy cases. The dashed and dash-dotted lines denote the wind parameterizations with* $n = 1/2$ *according to equations (5) and (6) respectively. The solid line denotes a linear increase of the transfer velocity as a function of the friction velocity [*Jähne et al.*, 1987]. (b) Transfer velocity constant* $k_{s,7}/u_*$ *according to equation (15) as a function of Ri. (Figure 6 and 7b in Paper III)*

3.6 Observational results at higher wind speeds, and speculations about the influence of waves

The transfer velocity estimations based on the flux-chamber and dissipation parameterization, and the quantities significant wave height (H_s), and IR surface velocity (V_{rms}) show a close relationship (Figure 18). The uncertainty in the dissipation parameterization, however, increased for low dissipation rates since the turbulence signal then was dominated by waves and instrument noise. Hence, transfer velocities using the dissipation parameterization that are below $2 \cdot 10^{-5}\ ms^{-1}$ are not presented in Figure 18. Nevertheless, a significant linear relationship was found between the transfer velocity estimations by the flux-chamber method and dissipation parameterizations and the significant wave height. A linear fit gave

$$k_{g,G2013,600} = (1.95 \cdot 10^{-4} \pm 4.9 \cdot 10^{-6})H_s + (4.9 \cdot 10^{-6} \pm 1.5 \cdot 10^{-6}). \quad (20)$$

No local wind measurements were available from the experiment, but it is reasonable to assume that the wave heights can be related to the wind speed and fetch, χ [e.g., *Hasselmann et al.*, 1976]. For a fetch of about 3 km, which is reasonable for the Bornö site at the given wind direction, this equation can be transformed into

$$k_{g,G2013,600} = (5.4 \cdot 10^{-6} \pm 3.7 \cdot 10^{-7})U_{10} + (4.8 \cdot 10^{-6} \pm 1.5 \cdot 10^{-6}). \quad (21)$$

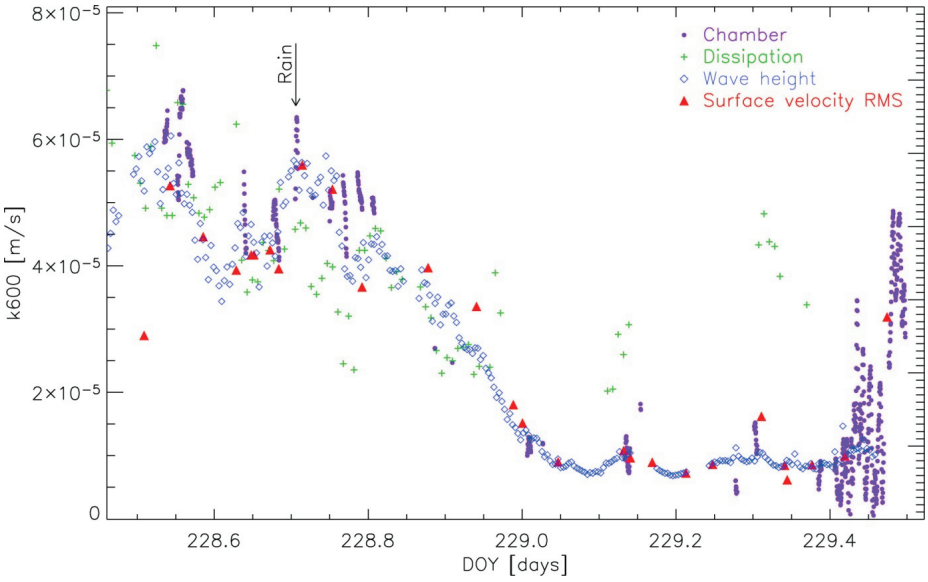

Figure 18. Comparison of transfer velocities using the flux-chamber method (filled circles), dissipation parameterization (plus signs), significant wave height (diamonds), and IR rms surface velocity (filled triangles). (Figure 7 in Paper IV).

The slope of equation (21) is close to the slope of $k_{g,J1987}$ for $n = 1/2$ and rather close to the transfer velocity forced by shear stress only, see section 3.7.3. It can therefore be argued that it actually is the shear stress rather than the waves that enhance the gas transfer velocity (elaborated in Paper III). If so, the significant wave height can still be a good proxy for the integrated effect of the shear stress, and thereby the gas flux, over the area of interest. In order to make equation (21) more general, the equation can be transformed to include the significant wave height and fetch (see Paper IV).

There was also a good correlation between the transfer velocity and the rms horizontal surface velocity estimated from PIV (from IR images). This can be expressed as

$$k_{g,rms,600} = A_{rms} \cdot V_{rms} + B_{rms} \qquad (22)$$

where A_{rms} and B_{rms} are constants. This close relationship for V_{rms} is unexpected since there is no direct relation between the rms horizontal surface velocity and the rms near-surface vertical velocity which may be expected to be important for gas exchange (see the discussion regarding solenoidal and irrotational components in section 3.4 and Figure 13). A reasonable explanation for the close $k - V_{rms}$ relationship may be found in the close relationship between the significant wave height and the transfer velocity, since estimated rms wave orbital velocities agree fairly well with V_{rms} from the IR/PIV-measurements. In that case, even this correlation is caused by the influence of wind stress on both gas transfer and waves.

One example of the temperature field used for PIV is shown in Figure 8 (from IR images). It shows a similar temperature pattern as the low shear-stress cases shown in Figure 15. Even though the DNS results show that the surface divergence

parameterization works well, the transfer velocity estimation using the surface divergence from the IR/PIV-measurement failed to give good correlation with the results from the other estimation methods. This is, however, most likely not due to problems with the divergence parameterization but rather the result of a need of finer spatial resolution of the velocity field in the IR/PIV method. Otherwise, the important small-scale divergence is not properly taken into account in the estimation of the total divergence.

3.7 Parameterizations of the gas transfer velocity

3.7.1 Based on diffusivity, surfactants, and shear-stress and buoyancy forcing

Paper I shows that the transfer velocity for pure buoyancy forcing is well represented by equation (18). It is here interesting to see the evident relationship to the buoyancy flux and that there is no influence of the depth for large enough depths. It can also be seen that the Schmidt exponent closely follows the theoretical derivation for slip and no-slip wall conditions. It should, though, be noted that the kinematic viscosity is included into equation (18) from dimensional considerations only and has not been altered in the analysis.

The parameterization for the combined forcing is more complex taking both the shear-stress and the buoyancy forcing into account. Paper III presents three different parameterizations. The rationale for three parameterizations is (i) that the users of the parameterizations might have specific needs for their implementation and (ii) that the parameterizations represent different ways of interpreting the physics. The first parameterization is based on a hypothesis that the forcings from buoyancy and shear stress are additive resulting in

$$\mathrm{k_{g,sum}} = \mathrm{A}_{Shear}\mathrm{u}_*(\mathrm{Ri}/\mathrm{Ri_c} + 1)^{1/4}\mathrm{Sc}^{-\mathrm{n}}, \tag{23}$$

where $\mathrm{Ri_c} = \left(A_{Shear}/A_{Buoy}\right)^4$ is a critical Richardson number and $A_{Shear} = 0.1$ is the transfer velocity coefficient for shear-stress forcing. It is based on the dissipation parameterization (equation (9)) and makes use of the fact that the forcings from buoyancy and shear scale as B and u_*^4/ν, respectively. This parameterization (equation (23)) is for $Q_0 =$ 50, 100, and 200 Wm^2 drawn in green in Figure 19.

The other two parameterizations are based on the hypothesis that the transfer velocity can be seen to be in two different states. The first state is buoyancy driven and the second state is shear-stress driven. The transition from one state to another is defined by a critical Richardson number. These two parameterizations either use an error function as

$$k_{g,erf} = \left[A_{Buoy}(B\nu)^{1/4} erf\left(\frac{Ri}{Ri_{c,erf}}\right) + A_{Shear}u_*\left(1 - erf\left(\frac{Ri}{Ri_{c,erf}}\right)\right)\right] Sc^{-n} \tag{24}$$

or a piecewise linear function as

$$k_g = \begin{cases} A_{Buoy}\,(Bv)^{1/4}\,Sc^{-n}, Ri > Ri_c \\ A_{Shear}\,u_*\,Sc^{-n}, Ri < Ri_c\,. \end{cases} \quad (25)$$

Equation (24) is drawn for $Q_0 =$ 50, 100, and 200 Wm^2 in red with $Ri_{c,erf} = 0.01$ and equation (25) is drawn for $Q_0 = 100$ in yellow in Figure 19. All three parameterizations (23)-(25) converge at high as well as low Ri.

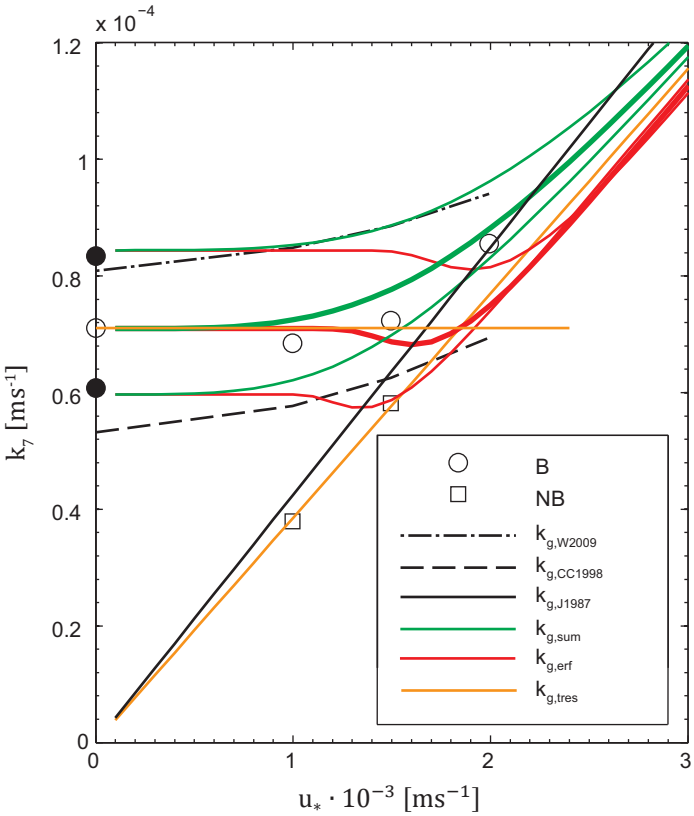

Figure 19. The gas transfer velocity constant $k_{g,7}$ according to equations (23) in green and (24) in red for $Q_0 =$ 50, 100, and 200 Wm^2. The scalar transfer velocities for pure buoyancy forcing with $Q_0 =$ 50 and 200 Wm^2 are marked with filled markers and were presented in Paper I. The transfer velocities for the pure buoyancy and shear forcing (equation (25)) are indicated in yellow. (Figure 9 in Paper III)

3.7.2 Based on dissipation, divergence, or heat flux

It was found in Paper I that the three parameterizations based on heat flux, dissipation, or divergence (equations(8)-(10)) give very good estimates of the transfer velocity for pure buoyancy forcing while varying the surface heat flux and domain depth. The values of the related transfer velocity coefficients are $A_{diss} = 0.45$, $A_{div} = 0.57$, and $A_{heat} = 0.90$.

The results for the parameterizations for the combined forcing in Paper III are, however, not as convincing as the results for buoyancy forcing only. This gives reason to be cautious in using the dissipation as a unifying quantity (proxy) that can be used to add different forcings into a total gas transfer parameterization. The relative variation $(A_{max} - A_{min})/A_{mean}$ is here used to rank the different parameterizations. The variation is for the cases $0B$ to $240B$ found to be approximately 10 %, 15%, and more than 35% for the heat, divergence, and the dissipation parameterizations respectively.

3.7.3 Based on the mean wind speed U_{10}

Figure 20 shows a number of parameterizations as functions of U_{10}. The parameterization in equation (23) is here plotted for surface heat fluxes in the range of $0 < Q_0 < 400\ Wm^{-2}$. The buoyancy flux influences the gas-transfer velocity up to approximately 2- 4 ms^{-1} according to additive parameterization, $\mathrm{k}_{g,\mathrm{sum}}$.

Furthermore, it is shown in Figures 19 and 20 that the two parameterizations based on the mean wind speed (equation (5) and (6)) give reasonable predictions of the transfer velocity for both the cases with pure natural convection and the combined forcing for a clean surface (slip). It can be seen that one parameterization [*Wanninkhof et al.*, 2009] overestimates and the other parameterization [*Cole and Caraco*, 1998] underestimates the transfer velocity compared to the base case with a surface heat flux of 100 Wm^{-2}. Congruent transfer velocities using equations (5) and (18) would imply a surface heat flux of approximately 35 Wm^{-2}, whilst equations (6) and (18) would imply approximately 200 Wm^{-2}. The surface heat flux is, however, in equations (5) and (6) not explicitly accounted for since the transfer velocity is a function of U_{10} only. For low wind conditions, it is therefore advisable to use any of equations (23)-(25) in order to have a parameterization that takes the buoyancy flux into account. It can further be seen that the two parameterizations (19) from wind tunnel tank test and equation (21) from field measurements give transfer velocities in the same magnitude.

Figure 20 also shows the large influence of the surfactants on the gas flux. There is a factor of approximately 3 between the transfer velocity for a clean surface (slip, $n \approx 1/2$) and for a surface that is saturated with surfactants (no-slip, $n \approx 2/3$) for $Sc = 600$.

Previous research has found that microscale breaking waves significantly contribute to the mean square slope of waves, which in turn can be correlated to the gas transfer velocity [*Zappa et al.*, 2002; 2004]. The gas transfer was found to be enhanced by a factor 3.5 comparing background levels and areas with microscale breakers. Furthermore, it is inferred that the microscale breaking may be the mechanism that enhances heat and mass transfer. The close agreement between the slopes in the parameterizations originating from wind tunnel tank measurements ($k_{g,J1987}$), using significant wave height ($k_{g,G2013}$), $k_{g,CC1998}$ and $k_{g,W2009}$, and equation (23) for clean conditions ($n = 1/2$) and $Q_0 = 0\ Wm^{-2}$ ($Ri = 0$) is therefore interesting in aspects of how large enhancement of the transfer-velocity waves and microscale breakers may give compared to pure shear-stress forcing, and is relevant to notice for future work

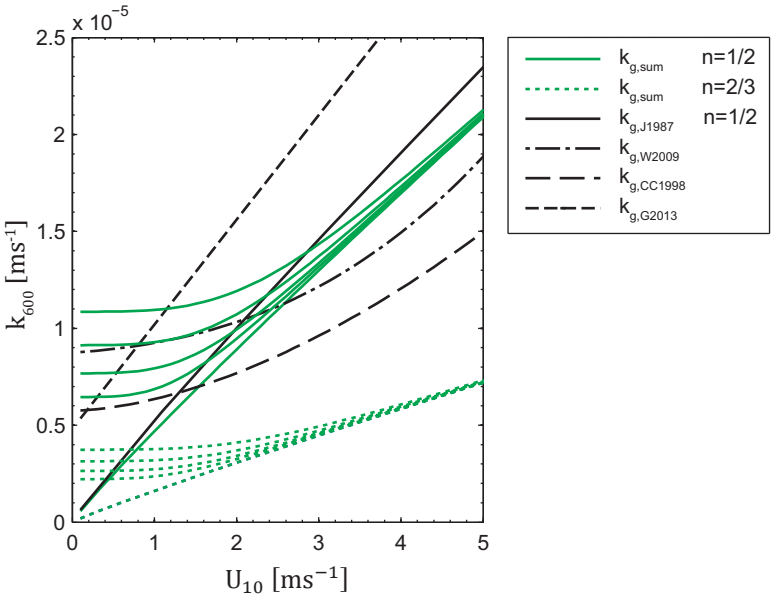

Figure 20. Transfer velocity constant $k_{g,600}$ according to equation (23) in green for $Q_0 = 0, 50, 100$, 200 and 400 Wm^2 and $n = 1/2$ (clean) and dotted line $n = 2/3$ (saturated surfactant). The parametrizations in equations (5-6), (19), and (21) are given for reference. The transfer velocity estimated with equation (6) is transformed into $Sc = 600$ using equation (7) and $n = 1/2$.

4 SUMMARY AND CONCLUSIONS

There is a growing need to determine the air-water gas exchange accurately during low wind conditions since (i) there is a general increase of the concentration and the interest in greenhouse gases e.g., CO_2 and CH_4 in the atmosphere, (ii) it has become evident that the gas fluxes from fresh-water bodies (where the wind speed often is low) play an important role in the global carbon cycle, and (iii) often used parameterizations based only on the wind speed cannot take other forcings as e.g., buoyancy into account.

New parameterizations for gas transfer velocity estimations have been developed by use of numerical simulations and field measurements in the ocean. The numerical simulations are performed as direct numerical simulations of fully developed turbulent flow for pure natural convective forcing, and combined convection and wind-shear forcing. The influence of surface heat flux, mixed layer depth, Schmidt number, and surfactants are evaluated. The field measurements comprise gas flux measurements by gas-flux chamber, IR/PIV-recording (e.g., surface flow divergence, rms surface velocity), and rate of turbulent kinetic energy dissipation in the water by acoustic doppler velocimetry.

The temperature and the surface-normal scalar flux fields at the surface show elongated streaks of warm and cold water (high and limited scalar flux) for the cases with pure shear stress forcing. The streak spacing is of the order of 100 ν/u_* (for pure

shear stress forcing) which previously has been seen for shear-stress driven flows, for both slip and no-slip surface boundary conditions. The temperature and the surface-normal scalar flux field are more complex for the combined forced cases. As shear is "added" to a pure natural-convection condition the plumes starts to be elongated and eventually as the shear stress is increased the streaks show a larger similarity with the pure shear-driven cases. This and the averaged statistics for all quantities studied indicate a transition from natural-convection (buoyancy) to shear-stress dominated flow at $Ri \approx 4 \cdot 10^{-3}$, which means that buoyancy fluxes are not important for gas exchange at wind velocities U_{10} above 3 ms^{-1}.

Parameterizations using the rate of turbulent kinetic energy dissipation, surface flow divergence, and heat flux, estimate the transfer velocity well for the cases with pure natural-convection, while varying the surface heat flux, domain depth, and Schmidt number. These parameterizations, however, experience some problems for the cases with combined convective and shear stress forcings. The relative variations in the transfer velocity are largest for the parameterization based on the dissipation rate and smallest for the parameterization based on the heat flux. The two parameterizations based on wind speed estimate the transfer velocities reasonable well, depending, however, on the surface heat flux. One parameterization [*Cole and Caraco,* 1998] corresponds to a heat flux of approximately 35 Wm^{-2} while the other [*Wanninkhof et al.*, 2009] corresponds to a heat flux of approximately 200 Wm^{-2}. Furthermore, there is no increase of transfer velocity as function of increasing domain depth (studied for pure convection forced case only).

The proposed new gas transfer parameterizations represent two different hypotheses. The first one assumes that the forcing from buoyancy and shear stress are additive. It uses the framework of the dissipation parameterization and sums the two dissipation scales for buoyancy and shear stress which results in the expression $k_{g,sum} = A_{Shear} u_* (Ri/Ri_c + 1)^{1/4} Sc^{-n}$ where the critical Richardson number $Ri_c = \left(A_{Buoy}/A_{Shear}\right)^4 \approx 4 \cdot 10^{-3}$.

The second one assumes that the forcing is either from the buoyancy or the shear stress. Here the transfer velocity is either modelled with a continuous error-function $k_{g,erf} = \left[A_{Buoy}(Bv)^{1/4} erf\left(\frac{Ri}{Ri_{c,erf}}\right) + A_{Shear} u_* erfc\left(\frac{Ri}{Ri_{c,erf}}\right)\right] Sc^{-n}$ where $Ri_{c,erf} = 0.01$. or with a piecewise linear function, that has a constant transfer velocity that equals the transfer due to buoyancy $k_{g,tres} = A_{Buoy}(Bv)^{1/4} Sc^{-n}$, for $Ri > Ri_c$ whereafter the transfer velocity due to shear according to the expression $k_{g,tres} = A_{Shear} u_* Sc^{-n}$ is used. The gas flux is to some extent overestimated by $k_{s,sum}$ and underestimated by $k_{s,tres}$ and $k_{s,erf}$. The maximum errors for the first two parameterizations are less than 10% and for the latter approximately 20%. The critical Richardson number in these parameterizations can be seen to express the transition point where the gas-flux forcing shifts from being dominated by either buoyancy or shear-stress. This implies that the buoyancy flux influence the gas transfer velocity up to approximately $U_{10} \approx 3\ ms^{-1}$ for natural conditions.

The results from the field measurements show close relationships for the method using flux-chambers and the parameterization using the rate of turbulent kinetic energy dissipation, and the quantities surface rms velocity and the significant wave height. These relationships can all be expressed as $k_g \propto U_{10}$ with a slope close to the results in the DNS for pure shear stress forcing and tests in a wind tank [*Jahne et al.*, 1987].

5 FUTURE PERSPECTIVES

The present work provides a firm ground for the understanding of gas flux across the air-water interface during low wind speed conditions. There are, though, still needs for future work for high Schmidt numbers and higher wind speeds. Although the results for high Schmidt number gases in Paper I are consistent regarding the gas transfer velocity, is still remains to be confirmed that these are valid for a computational mesh with higher resolution as well. This can be achieved in a similar way as *Herlina and Wissink* [2014] who used two different meshes with different mesh resolutions for solving the flow field and the scalar field.

It would also be fruitful to continue the work towards more accurate gas transfer estimations for higher wind speeds. The next step is then to perform direct numerical simulations in order to study the mechanisms of e.g., microscale-breaking and breaking waves. This has to some extent been done [e.g., *Lin et al.*, 2008; *Tsai and Hung*, 2007] but there is still a need for a comprehensive parameter study including the influence of surfactants.

Furthermore it would be interesting to study how the concept of turbulence-surfactant parameter can be used in field work and how the surfactant concentration and the surface elasticity can be estimated?

Eventually it would be worthwhile to study whether the temperature field recorded with an IR camera can obtain high enough resolution to capture the important small-scale divergence at the surface.

ACKNOWLEDGEMENTS

Now I would like to take the opportunity to acknowledge my supervisors, colleagues, friends and family, who have supported me during my studies and this PhD project.

First, I would like to express my sincere gratitude to my supervisor, Lars Arneborg, and co-supervisor, David Bastviken. I have always felt a very supportive attitude from them, and been encouraged by their competence and eagerness to learn and explore new things. I would also like to express my sincere gratitude to Robert Handler and Håkan Nilsson who both have been very encouraging during the work leading up to this thesis. The meetings with Robert (by wire, in Texas, or in Gothenburg) have always been a source of large inspiration to me. Håkan has been a very valuable guide during my exploration and eventually programming of OpenFOAM. I would also like to express my appreciation to the remaining co-authors of jointly written papers during my studies. It has e.g., been inspiring to see the fascinating IR-images by one of the co-authors, Magnus Gålfalk. Many thanks also to the group of gas-flux researchers from the Uppsala University for nice field work and fruitful discussions.

I would also like to thank Ola Kalen, a companion at several conferences who I have shared office with for several years. Beside the work it has been inspiring to talk about our common interests outside the academia. Thanks also; to Ardo Robijn for being my fellow researcher at the expeditions to the areas at and around Svalbard, to Anna Wåhlin for making our participating in that research project (PREPARED) possible, and to all of the members of these memorable research cruises. The list of colleagues to thank could be as long as a movie credit. However, due to space limits, let me just send my general and genuine thanks to all the colleagues at GU not mentioned here but still remembered and all of you who have become dear friends of mine during my studies.

A good life outside the office is of great importance for me and for the success of my work, and I am lucky to have many wonderful people around me. First I would like to thank Anna for her support, joy, and ultimately even some help with the final formatting of this thesis. I would then like to give my wholehearted thanks; to mom and dad for their caring and unconditional support to me and the family, and to my brother for many good times together. Great thanks to Kristina and Anders for all their journeys to Gothenburg during these years. I am also very grateful for the large and caring ring of friends that bring me so much friendship and enjoyment.

Eventually I would like to send a heap of hugs to my lovely children Sara, Martin, and Emil. You have been very patient during this spring and you always bring me so much joy!

I would also like to acknowledge Semcon who gave me study leave to fulfil this PhD project. The computations were performed on resources provided by the Swedish National Infrastructure for Computing (SNIC) at C3SE (Chalmers Centre for Computational Science and Engineering) computing resources. My supervisor Lars Arneborg was supported by the Swedish Research Council.

REFERENCES

Bade, D. L. (2009), Gas Exchange at the Air–Water Interface, in *Encyclopedia of Inland Waters*, edited by G. E. Likens, pp. 70-78, Academic Press, Oxford,http://dx.doi.org/10.1016/B978-012370626-3.00213-1.

Banerjee, S., D. S. Scott, and E. Rhodes (1968), Mass Transfer to Falling Wavy Liquid Films in Turbulent Flow, *Ind Eng Chem Fund*, *7*(1), 22-&,Doi 10.1021/I160025a004.

Banerjee, S., D. Lakehal, and M. Fulgosi (2004), Surface divergence models for scalar exchange between turbulent streams, *Int J Multiphas Flow*, *30*(7-8), 963-977,DOI 10.1016/j.imultiphase.2004.05.004.

Bastviken, D., L. J. Tranvik, J. A. Downing, P. M. Crill, and A. Enrich-Prast (2011), Freshwater Methane Emissions Offset the Continental Carbon Sink, *Science*, *331*(6013), 50-50,DOI 10.1126/science.1196808.

Calmet, I., and J. Magnaudet (1998), High-Schmidt number mass transfer through turbulent gas-liquid interfaces, *Int J Heat Fluid Fl*, *19*(5), 522-532,Doi 10.1016/S0142-727x(98)10017-6.

Ciais, P., et al. (2013), Carbon and Other Biogeochemical Cycles. In: Climate Change 2013: The Physical Science Basis. Contribution of Working Group I to the Fifth Assessment Report of the Intergovernmental Panel on Climate Change*Rep.*, 465–570 pp, Cambridge University Press, Cambridge, United Kingdom and New York, NY, USA,10.1017/CBO9781107415324.015.

Cole, J. J., and N. F. Caraco (1998), Atmospheric exchange of carbon dioxide in a low-wind oligotrophic lake measured by the addition of SF6, *Limnol Oceanogr*, *43*(4), 647-656

Cole, J. J., D. L. Bade, D. Bastviken, M. L. Pace, and M. Van de Bogert (2010), Multiple approaches to estimating air-water gas exchange in small lakes, *Limnology and Oceanography: Methods*, *8*(6), 285-293,10.4319/lom.2010.8.285.

Csanady, G. T. (2001), *Air-sea interaction : laws and mechanisms*, vii, 239 p. pp., Cambridge University Press, Cambridge ; New York

Fairall, C. W., E. F. Bradley, J. S. Godfrey, G. A. Wick, J. B. Edson, and G. S. Young (1996), Cool-skin and warm-layer effects on sea surface temperature, *J Geophys Res-Oceans*, *101*(C1), 1295-1308,Doi 10.1029/95jc03190.

Fortescue, G. E., and J. R. A. Pearson (1967), On Gas Absorption into a Turbulent Liquid, *Chem Eng Sci*, *22*(9), 1163-&,Doi 10.1016/0009-2509(67)80183-0.

Frew, N. M., et al. (2004), Air-sea gas transfer: Its dependence on wind stress, small-scale roughness, and surface films, *J Geophys Res-Oceans*, *109*(C8),Artn C08s17,Doi 10.1029/2003jc002131.

Garbe, C. S. (2001), Measuring heat exchange processes at the air-water interface from thermographic image sequence analysis, 232 pp, Rupertus Carola University of Heidelberg, Heidelberg

Garbe, C. S., H. Spies, and B. Jahne (2003), Estimation of surface flow and net heat flux from infrared image sequences, *J Math Imaging Vis*, *19*(3), 159-174,Doi 10.1023/A:1026233919766.

Garratt, J. R. (1992), *The atmospheric boundary layer*, Cambridge University Press

Handler, R. A., G. B. Smith, and R. I. Leighton (2001), The thermal structure of an air-water interface at low wind speeds, *Tellus A*, *53*(2), 233-244

Hasegawa, Y., and N. Kasagi (2008), Systematic analysis of high Schmidt number turbulent mass transfer across clean, contaminated and solid interfaces, *Int J Heat Fluid Fl*, *29*(3), 765-773,DOI 10.1016/j.ijheatfluidflow.2008.03.002.

Hasselmann, K., W. Sell, D. B. Ross, and P. Müller (1976), A Parametric Wave Prediction Model, *J Phys Oceanogr*, *6*(2), 200-228,10.1175/1520-0485(1976)006<0200:APWPM>2.0.CO;2.

Haussecker, H., U. Schimpf, and B. Jahne (1998), Measurements of the air-sea gas transfer and its mechanisms by active and passive thermography, *Igarss '98 - 1998 International Geoscience and Remote Sensing Symposium, Proceedings Vols 1-5*, 484-486,Doi 10.1109/Igarss.1998.702947.

Herlina, H., and J. G. Wissink (2014), Direct numerical simulation of turbulent scalar transport across a flat surface, *J Fluid Mech*, *744*, 217-249,Doi 10.1017/Jfm.2014.68.

Jahne, B., and H. Haussecker (1998), Air-water gas exchange, *Annu Rev Fluid Mech*, *30*, 443-468

Jahne, B., P. Libner, R. Fischer, T. Billen, and E. J. Plate (1989), Investigating the transfer processes across the free aqueous viscous boundary layer by the controlled flux method, *Tellus B*, *41*(2), 177-195,DOI 10.1111/j.1600-0889.1989.tb00135.x.

Jahne, B., K. O. Munnich, R. Bosinger, A. Dutzi, W. Huber, and P. Libner (1987), On the Parameters Influencing Air-Water Gas-Exchange, *J Geophys Res-Oceans*, *92*(C2), 1937-1949

Jerlov, N. G. (1976), *Marine Optics*, Elsevier Science

Kara, A. B., P. A. Rochford, and H. E. Hurlburt (2000), An optimal definition for ocean mixed layer depth, *Journal of Geophysical Research: Oceans*, *105*(C7), 16803-16821,10.1029/2000JC900072.

Kim, J., and P. Moin (1989), Transport of Passive Scalars in a Turbulent Channel Flow, in *Turbulent Shear Flows 6*, edited by J.-C. André, J. Cousteix, F. Durst, B. Launder, F. Schmidt and J. Whitelaw, pp. 85-96, Springer Berlin Heidelberg,10.1007/978-3-642-73948-4_9.

Kim, J., P. Moin, and R. Moser (1987), Turbulence Statistics in Fully-Developed Channel Flow at Low Reynolds-Number, *J Fluid Mech*, *177*, 133-166,Doi 10.1017/S0022112087000892.

Lamont, J. C., and D. S. Scott (1970), An Eddy Cell Model of Mass Transfer into Surface of a Turbulent Liquid, *Aiche J*, *16*(4), 513-&

Ledwell, J. J. (1984), The Variation of the Gas Transfer Coefficient with Molecular Diffusity, in *Gas Transfer at Water Surfaces*, edited by W. Brutsaert and G. H. Jirka, pp. 293-302, Springer Netherlands, Dordrecht,10.1007/978-94-017-1660-4_27.

Lin, M. Y., C. H. Moeng, W. T. Tsai, P. P. Sullivan, and S. E. Belcher (2008), Direct numerical simulation of wind-wave generation processes, *J Fluid Mech*, *616*, 1-30,Doi 10.1017/S0022112008004060.

Macintyre, S., W. Eugster, and G. W. Kling (2002), The Critical Importance of Buoyancy Flux for Gas Flux Across the Air-Water Interface, in *Gas Transfer at Water Surfaces*, edited, pp. 135-139, American Geophysical Union,10.1029/GM127p0135.

McKenna, S. P., and W. R. McGillis (2004), The role of free-surface turbulence and surfactants in air-water gas transfer, *Int J Heat Mass Tran*, *47*(3), 539-553,DOI 10.1016/j.ijheatmasstransfer.2003.06.001.

Monahan, A. H. (2006), The probability distribution of sea surface wind speeds. Part 1: Theory and SeaWinds observations, *J Climate*, *19*(4), 497-520,Doi 10.1175/Jcli3640.1.

Ohlmann, J. C., D. A. Siegel, and C. D. Mobley (2000), Ocean radiant heating. Part I: Optical influences, *J Phys Oceanogr*, *30*(8), 1833-1848,Doi 10.1175/1520-0485(2000)030<1833:Orhpio>2.0.Co;2.

Read, J. S., et al. (2012), Lake-size dependency of wind shear and convection as controls on gas exchange, *Geophys Res Lett*, *39*,Artn L09405,Doi 10.1029/2012gl051886.

Rutgersson, A., and A. Smedman (2010), Enhanced air-sea CO2 transfer due to water-side convection, *J Marine Syst*, *80*(1-2), 125-134,DOI 10.1016/j.jmarsys.2009.11.004.

Soloviev, A. X., and P. Schlussel (1994), Parameterization of the Cool Skin of the Ocean and of the Air Ocean Gas Transfer on the Basis of Modeling Surface Renewal, *J Phys Oceanogr*, *24*(6), 1339-1346

Stewart, R. W. (2008), *Introduction to physical oceanography*, September 2008 ed.

Takahashi, T., et al. (2009), Climatological mean and decadal change in surface ocean pCO2, and net sea–air CO2 flux over the global oceans, *Deep Sea Research Part II: Topical Studies in Oceanography*, *56*(8–10), 554-577,http://dx.doi.org/10.1016/j.dsr2.2008.12.009.

Tranvik, L. J., et al. (2009), Lakes and reservoirs as regulators of carbon cycling and climate, *Limnol Oceanogr*, *54*(6), 2298-2314,DOI 10.4319/lo.2009.54.6_part_2.2298.

Tsai, W. T., and L. P. Hung (2007), Three-dimensional modeling of small-scale processes in the upper boundary layer bounded by a dynamic ocean surface, *J Geophys Res-Oceans*, *112*(C2),Artn C02019,Doi 10.1029/2006jc003686.

Wanninkhof, R., W. E. Asher, D. T. Ho, C. Sweeney, and W. R. McGillis (2009), Advances in Quantifying Air-Sea Gas Exchange and Environmental Forcing, *Annu Rev Mar Sci*, *1*, 213-244,DOI 10.1146/annurev.marine.010908.163742.

Veron, F., W. K. Melville, and L. Lenain (2008), Infrared techniques for measuring ocean surface processes, *J Atmos Ocean Tech*, *25*(2), 307-326,Doi 10.1175/2007jtech0524.1.

Wick, G. A., J. C. Ohlmann, C. W. Fairall, and A. T. Jessup (2005), Improved Oceanic Cool-Skin Corrections Using a Refined Solar Penetration Model, *J Phys Oceanogr*, *35*(11), 1986-1996,10.1175/JPO2803.1.

Volino, R. J., and G. B. Smith (1999), Use of simultaneous IR temperature measurements and DPIV to investigate thermal plumes in a thick layer cooled from above, *Exp Fluids*, *27*(1), 70-78

Zappa, C. J., P. A. Raymond, E. A. Terray, and W. R. McGillis (2003), Variation in surface turbulence and the gas transfer velocity over a tidal cycle in a macro-tidal estuary, *Estuaries*, *26*(6), 1401-1415,Doi 10.1007/Bf02803649.

Zappa, C. J., W. E. Asher, A. T. Jessup, J. Klinke, and S. R. Long (2002), Effect of Microscale Wave Breaking on Air-Water Gas Transfer, in *Gas Transfer at Water Surfaces*, edited, pp. 23-29, American Geophysical Union,10.1029/GM127p0023.

Zappa, C. J., W. E. Asher, A. T. Jessup, J. Klinke, and S. R. Long (2004), Microbreaking and the enhancement of air-water transfer velocity, *J Geophys Res-Oceans*, *109*(C8),Artn C08s16,Doi 10.1029/2003jc001897.

Zappa, C. J., W. R. McGillis, P. A. Raymond, J. B. Edson, E. J. Hintsa, H. J. Zemmelink, J. W. H. Dacey, and D. T. Ho (2007), Environmental turbulent mixing controls on air-water gas exchange in marine and aquatic systems, *Geophys Res Lett*, *34*(10),Artn L10601,Doi 10.1029/2006gl028790.

Part B

Papers I–IV